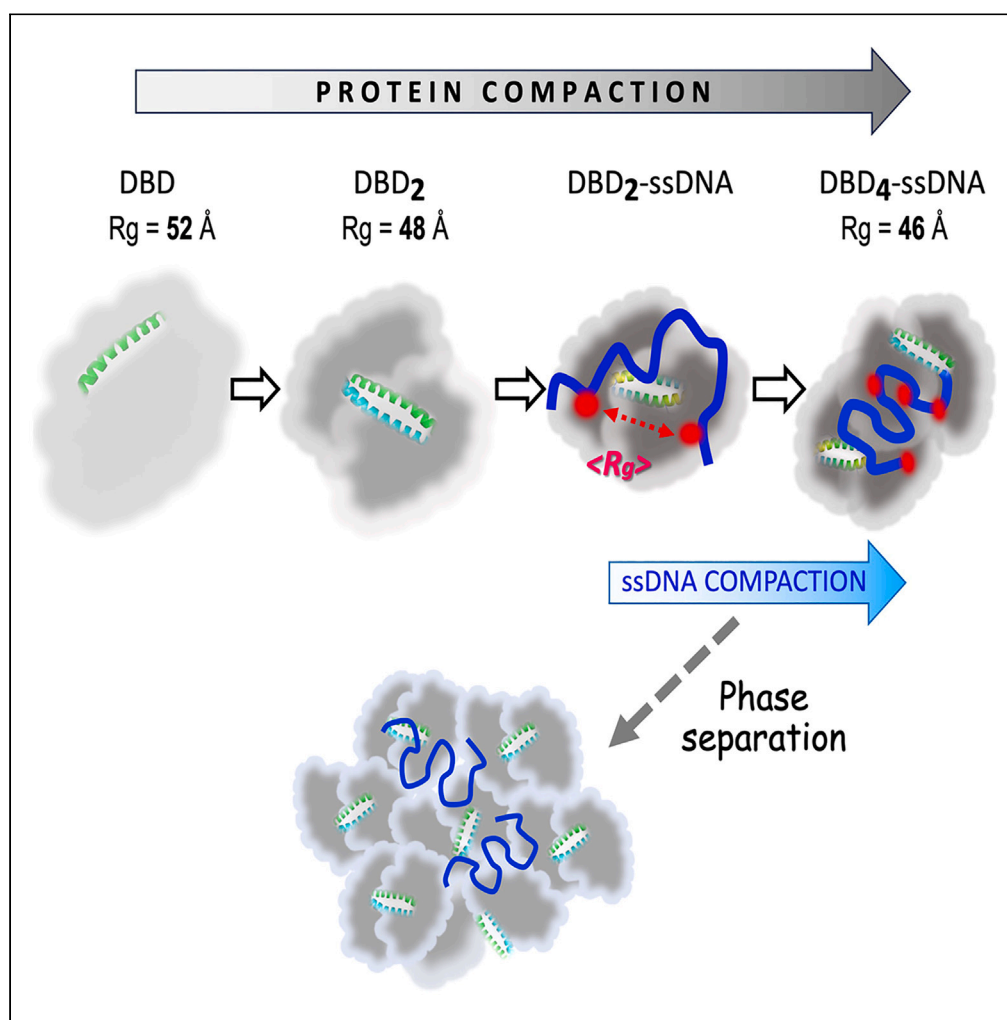# iScience

Article

The strand exchange domain of tumor suppressor PALB2 is intrinsically disordered and promotes oligomerization-dependent DNA compaction

Yevhenii Kyriukha, Maxwell B. Watkins, Jennifer M. Redington, ..., Jesse B. Hopkins, Nicola Pozzi, Sergey Korolev

sergey.korolev@health.slu.edu

Highlights

PALB2-DBD is intrinsically disordered in monomeric, oligomeric and DNA-bound states

PALB2-DBD is compacted 2-fold upon dimerization and 4-fold upon tetramerization

PALB2-DBD promotes bimodal oligomerization-dependent compaction of ssDNA

IDR stabilizes oligomerization and promotes salt- and DNA-dependent phase separation

Article

The strand exchange domain of tumor suppressor PALB2 is intrinsically disordered and promotes oligomerization-dependent DNA compaction

Yevhenii Kyriukha,[1,4] Maxwell B. Watkins,[2,4] Jennifer M. Redington,[1,4] Nithya Chintalapati,[1] Abhishek Ganti,[1] Reza Dastvan,[1] Vladimir N. Uversky,[3] Jesse B. Hopkins,[2] Nicola Pozzi,[1] and Sergey Korolev[1,5,*]

SUMMARY

The partner and localizer of BRCA2 (PALB2) is a scaffold protein linking BRCA1 with BRCA2 and RAD51 during homologous recombination (HR). PALB2 interaction with DNA strongly enhances HR in cells, while the PALB2 DNA-binding domain (PALB2-DBD) supports DNA strand exchange *in vitro*. We determined that PALB2-DBD is intrinsically disordered beyond a single N-terminal α-helix. Coiled-coil mediated dimerization is stabilized by interaction between intrinsically disordered regions (IDRs) leading to a 2-fold structural compaction. Single-stranded (ss)DNA binding promotes additional structural compaction and protein tetramerization. Using confocal single-molecule FRET, we observed bimodal and oligomerization-dependent compaction of ssDNA bound to PALB2-DBD, suggesting a novel strand exchange mechanism. Bioinformatics analysis and preliminary observations indicate that PALB2 forms protein-nucleic acids condensates. Intrinsically disordered DBDs are prevalent in the human proteome. PALB2-DBD and similar IDRs may use a chaperone-like mechanism to aid formation and resolution of DNA and RNA multichain intermediates during DNA replication, repair and recombination.

INTRODUCTION

Homologous recombination (HR) is essential for the exchange of genetic information between maternal and paternal alleles and proper chromosome segregation during meiosis, for non-mutagenic repair of large chromosome aberrations such as double-stranded (ds) DNA breaks (DSB), for repair of stalled replication forks, and for a plethora of other DNA transactions.[1–4] HR is almost exclusively supported by a single family of RecA-like recombinases, including phage UvsX, bacterial RecA, archaea RadA, and eukaryotic Rad51 and DMC1.[5] The sequences and structures of these RecA-like recombinases are highly conserved, owing to the complexity of a multistep HR reaction involving the formation of an ATP-dependent protein filament on single-stranded (ss) DNA that is capable of searching for a homologous dsDNA and catalyzing strand displacement and strand exchange.[3,6–8] The complexity of this mechanism limits the evolution of more specialized recombinases. Numerous partner proteins have evolved to regulate organism- and pathway-specific activities of RecA-like recombinases at multiple levels.[9–13] RecA-like recombinases recombine long DNA regions with high fidelity but are not efficient for strand exchange between short DNA fragments or between DNA and RNA that may be required during replication fork reversal or transcription/replication collision. Another protein capable of strand exchange is the eukaryotic Rad52,[14–16] which is also a major positive regulator of Rad51 in yeast.[17,18] Rad52 forms an oligomeric toroidal ring that binds ssDNA and dsDNA to promote promiscuous strand exchange.[19–21] Rad52 is more efficient than Rad51 in strand exchange between RNA and DNA and is proposed to repair breaks that occur during collision of replication with transcription using newly transcribed mRNA as a homologous template.[14,22] Other protein families, such as *E. coli* RecE/RecT, bacteriophage λ Redα/ Redβ, and viral UL12/ICP8 complexes,[8,23–25] are reported to support DNA recombination, although through the combination of exonuclease and strand annealing rather than strand exchange mechanism.[26] The described proteins form ring-shaped oligomers.[27,28] The necessity to process complex multichain DNA and RNA intermediates that are formed in chromatin during all major nucleic acid metabolism reactions is further underscored by limited reports of other proteins with strand annealing and exchange activities. These families include the FANCA protein of the Fanconi anemia (FA) complex, which is critical for DNA interstrand crosslink repair,[29] and the RNA-processing FET proteins such as pro-oncoprotein TLS/FUS and the human splicing factor PSF/hPOMp100.[30–32]

We discovered that the Partner And Localizer of BRCA2 (PALB2) protein facilitates DNA and RNA strand exchange.[33] Human PALB2 is a scaffold protein (1186 amino acids) that links BRCA1 and BRCA2 during HR initiation, where BRCA2 stimulates RAD51 filament formation.[34–40]

PALB2 interacts with numerous other chromatin and transcription factors, and with RAD51 and its paralogs.[35] The N-terminal domain encompassing amino acids 1–195 interacts with DNA (referred to hereafter as PALB2-DBD) (Figure 1A).[41,42] Alanine substitution of major DNA-binding amino acids 146-RRKK-149 decreases radiation-induced RAD51 foci and HR in cells by 50%.[33] We discovered that PALB2-DBD alone promotes RAD51-independent strand exchange *in vitro*.[33] PALB2 lacks any sequence or similarities with Rad51 or Rad52, and likely uses a novel mechanism for strand exchange.

Here, we present evidence that PALB2-DBD is an intrinsically disordered domain (IDD) or region (IDR), which forms a compact dimer stabilized by coiled-coil interaction and the attraction between IDRs, and which undergoes DNA-dependent tetramerization. Single-stranded (ss) DNA binding further compacts the structure and ssDNA itself is condensed upon binding even in the absence of secondary structure elements. The described oligomerization-dependent DNA condensation and previously reported strand exchange activity by the same domain significantly expands the structural and functional repertoire of intrinsically disordered proteins (IDPs), which represent a third of the human proteome.[43] Approximately 30% and 50% of protein and RNA chaperones are estimated to form IDRs, and the proposed strand exchange mechanism will have broad implications as only a few have been mechanistically characterized.[44–46] Many eukaryotic DNA repair proteins such as BRCA1 and BRCA2 contain DNA-binding IDRs of unknown function. We hypothesize that such regions represent a novel functional class of DNA repair effectors that can aid transactions between DNA and RNA strands to form or resolve local transient multistrand intermediates that occur near stalled replication forks, DNA breaks and other chromosomal aberrations.

RESULTS

PALB2-DBD is comprised of a low complexity amino acid sequence with predicted context-dependent folding

PALB2-DBD sequence includes the N-terminal α-helix (aa 10–40)[47] that forms an antiparallel coiled-coil either with itself (referred to hereafter as PALB2-cc) to form a homodimer, or with the BRCA1 α-helix[48–50] (Figure 1A). The remaining part comprises a low complexity sequence, typical for scaffold proteins, with several short low propensity α-helical regions (https://MobiDB.bio.unipd.it/Q86YC2 and https://alphafold.ebi.ac.uk/entry/Q86YC2).[51,52] However, several properties of PALB2-DBD, such as dimerization, localized DNA binding site, and complex strand exchange activity, are not typically associated with disordered proteins. Moreover, the fragment is also relatively soluble under physiological conditions and is proteolysis-resistant during purification. This suggests that that oligomerization and/or DNA binding can stimulate the formation of additional α-helixes and folding. Charge-hydropathy plot[53,54] generated using PONDR server (www.pondr.com) places the sequence close to the folded/disordered boundary (Figure 1B). The PALB2-DBD is a neutral peptide with a balanced content of hydrophobic, positively, and negatively charged amino acids distributed alone the entire sequence (Figures 1C and 1D), as calculated using CIDER analysis,[55] and characteristic for a context-dependent structural organization.[55–59] Δ40-DBD sequence (amino acids 41-195) is placed at the boundary between "Janus sequences: Collapsed or expanded–context dependent" and "Weak polyampholytes & polyelectrolytes: Globule & tadpoles." Analysis of this protein by the flDPnn platform (http://biomine.cs.vcu.edu/servers/flDPnn/), designed for the accurate intrinsic disorder prediction with putative propensities of disorder functions,[60] further supports the excessive disorder-based interactivity of PALB2-DBD, predicting multiple regions with a strong propensity for protein binding as well as DNA and RNA interactions.

PALB2-DBD sequence analysis using RIDAO server (https://ridao.app/)[61] which utilizes several predictors (mean disorder profile (MDP) error; PONDRs VLXT, VL3 and VSL2, IUPred-Long, IUPred-Short and PONDR-FIT) suggest a mostly disordered structure (Figure 1E), while multiple segments of the domain (aa 5–46, 49–58, 70–79, 86–100, 118–129, 135–143, 145–167, and 174–194) were identified by FuzPred (https://fuzdrop.bio.unipd.it/predictor)[62,63] as regions with context-dependent interactions (Figure 1F). Furthermore, the PALB2-DBD is predicted to contain six disorder-based protein-protein interaction sites (aa 18–35, 74–86, 98–106, 113–118, 154–174, and 193–206) known as molecular recognition features (MoRFs), which are IDRs undergoing binding-induced folding upon interaction with specific partners[64–69] (Figures S1A and S1B). Thus, the sequence analysis does not rule out potential context-dependent folding that may be required for novel strand exchange mechanism. Therefore, we used several experimental approaches to characterize the PALB2-DBD structure.

PALB2-DBD structure is highly flexible, lacking stable secondary structure elements beyond the N-terminal α-helix with and without DNA

We utilized circular dichroism (CD) spectroscopy to analyze the content of secondary structure elements (Figure 2). The PALB2-DBD spectra are characterized by peaks corresponding to α-helical (223 nm) and disordered (204 nm) structures (Figure 2A, solid line). The spectrum of the Δ40-DBD fragment lacking the N-terminal α-helix does not display a peak corresponding to α-helix (Figure 2B). Therefore, CD spectroscopy did not detect secondary structure elements beyond the N-terminal coiled-coil region in PALB2-DBD. To investigate whether additional secondary structure elements can be stabilized by interactions with DNA, we measured CD spectra from PALB2-DBD and Δ40-DBD in the presence of excess ssDNA (dT$_{50}$) (Figures 2A and 2B, dashed lines) at buffer conditions compatible with DNA binding (Figure S2).

The results showed that neither PLAB2-DBD nor Δ40-DBD spectra were altered by addition of ssDNA. While this qualitative analysis does not rule out the presence of minor and/or transitional secondary structure elements nor the potential formation of additional α-helixes upon coiled-coil–mediated oligomerization of PALB2-DBD, it suggests that Δ40-DBD lacks stable secondary structure elements and folding even upon DNA binding, despite a localized major DNA-binding site typical for globular proteins.

As IDRs are characterized by high flexibility, we analyzed the local flexibility of different regions using continuous wave electron paramagnetic resonance (cwEPR) spectroscopy (Figures 3A–3C), which is particularly informative for structural characterization of IDPs and their interactions.[70,71] Four cysteines in human PALB2-DBD were alternatively substituted by alanines to create single cysteine variants at positions 11, 57, 77, and 162 (Figure 3D). Lack of cysteines did not alter DNA binding properties of PALB2-DBD (Figure S2A). Two additional cysteines were
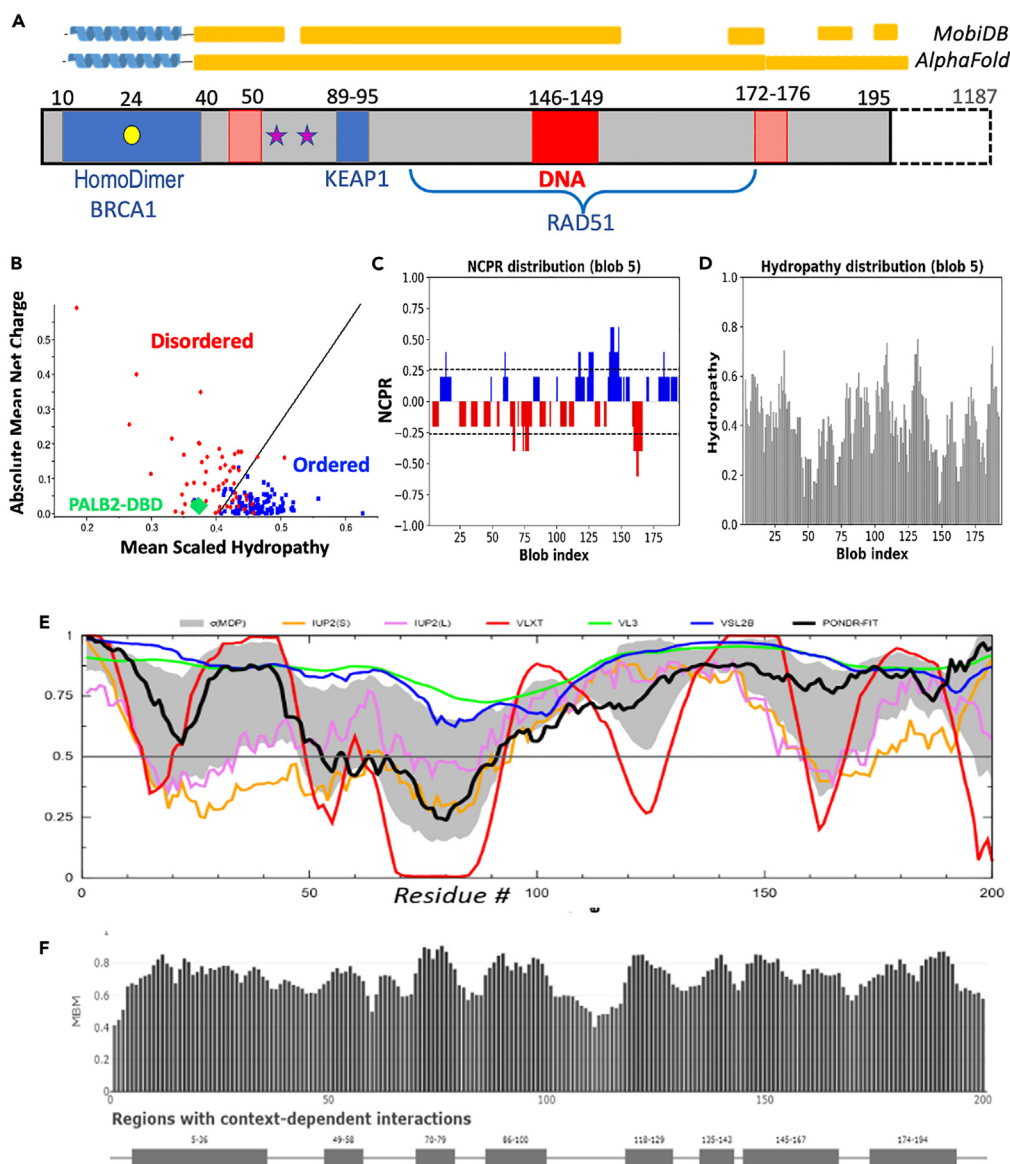
Figure 1. Amino acid sequence features of PALB2-DBD

(A) PALB2 sequence motifs. Amino acid sequence numbers are shown above each domain. Shadowed area, PALB2-DBD; blue area, known protein interaction sites; red area, major DNA-binding site; pink area, minor DNA-binding sites; stars, phosphorylation sites; yellow bars above, disordered regions according to MobiDB or AlphaFold prediction.

(B) Charge-hydropathy plot generated using PONDR server (www.pondr.com).

(C and D) CIDER analysis (http://157.245.85.131:8000/CIDER/) of charge distribution plotted as net charge distribution (NCPR) (C) and hydrophobicity (D).

(E) Plot of disorder score against residues number using RIDAO server accordingly to following predictors: mean disorder profile (MDP) error; PONDRs VLXT, VL3 and VSL2, IUPpred-Long, IUPred-Short and PONDR-FIT.

(F) Multiplicity of binding modes evaluated by FuzPred (https://fuzdrop.bio.unipd.it/predictor).

introduced in the vicinity of the major DNA-binding site (S136C, S145C). The nitroxide-containing spin label 1-oxyl-2,2,5,5-tetramethyl-d3-pyrroline-3-methyl methane thiosulfonate (MTSSL) was covalently attached to the cysteine thiol group for EPR analysis. The EPR spectrum was measured for each mutant alone (Figure 3A) and in the presence of ssDNA (Figures 3B and 3C). Most spectra correspond to a highly flexible conformation of local peptide in the label vicinity. Values of the h(+1)/h(0) ratio correspond to those for other IDPs (Figure 3C),[71] with the exception of position 11 at the beginning of the PALB2-cc where a lower value corresponds to a more rigid structure near the coiled-coil region. The overall tumbling rate of the complex (dimer molecular weight of 47 kDa) is too slow to affect the EPR spectrum. The antiparallel coiled-coil structure was previously detected for isolated α-helixes by NMR.[47] To confirm that this interaction is preserved
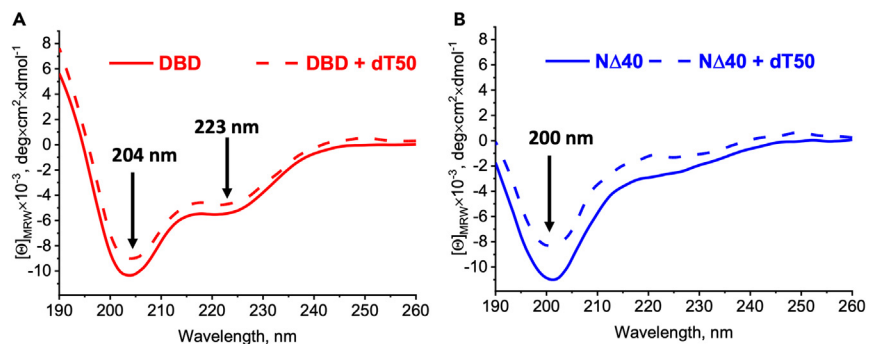
Figure 2. CD spectroscopy of PALB2-DBD

CD spectra of PALB2-DBD (A), and of Δ40-DBD (B). Solid lines correspond to the protein alone at 30 mM and dashed to the protein in the presence of 30 mM dT$_{50}$. Spectrum were obtained in a buffer 10 mM Sodium Phosphate, 150 mM NaF, 2 mM CHAPS.

within the entire PALB2-DBD, we used DEER spectroscopy of protein labeled at position 11 (Figures 3E and 3F). The measured distance of 47.3 Å is in good agreement with theoretical distribution calculated using NMR structure (Figure 3E, insert).

The addition of dT$_{40}$ causes a notable change in flexibility only at position 145 immediately next to the major DNA-binding site (146–149 aa) and a minor decrease at position 136 proximal to DNA binding site (Figures 3B and 3C). Both regions are still more flexible even in the pres-ence of DNA than the coiled-coil region (position 11). There was no change in local flexibility at other labeled positions (Figure 3C). Thus, DNA binding does not affect structural flexibility beyond the immediate vicinity of the major DNA-binding site. High flexibility of the probed re-gions further confirms a lack of secondary structures formed inside the Δ40-DBD sequence, even within the oligomeric PALB2-DBD and in the DNA-bound state. The combined results indicate that PALB2-DBD has an intrinsically disordered and highly flexible structure beyond the N-terminal α-helix.

A dimerization-dependent compaction of PALB2-DBD

IDPs have different functionally relevant structural organizations ranging from compact molten globule (MG) structures to extended random coil (RC) conformations, which can be distinguished by a hydrodynamic volume (V_h) that is only 2–3 times larger than the volume of a folded globular structure of the same molecular weight for MG and up to 10 times larger for RC.[72] Since the PALB2-DBD structural organization is
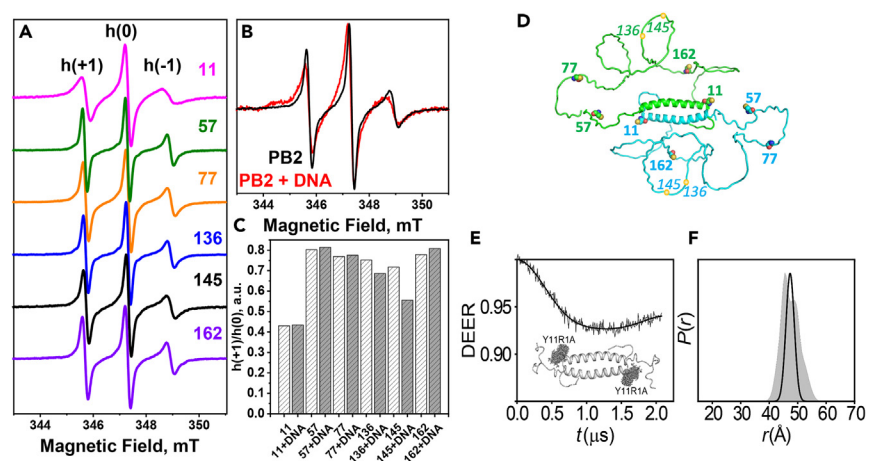

Figure 3. Continuous wave EPR and DEER spectroscopy of PALB2-DBD

(A) cwEPR spectra of PALB2-DBD labeled at different positions indicated by the number on the right.

(B) Overlay of PALB2-DBD spectra labeled at position 145 in free (black) and DNA-bound (red) states.

(C) h(+1)/h(0) values for the labeled positions from spectra shown in (A). Dark gray bars correspond to the signal in the presence of DNA. cwEPR data were obtained with 30 mM protein and 60 mM dT$_{40}$ in buffer with 20 mM Tris-acetate pH 7, 100 mM NaCl, 10% DMSO, and 5% glycerol.

(D) Hypothetical conformation of PALB2-DBD dimer generated by the AlphaFold program. Monomers are shown in cyan and green. Cysteine positions used for labeling are marked with spheres and aa numbers.

(E) Raw DEER decay for the PALB2-DBD labeled at position 11 with fitting for the experimentally determined P(r).

(F) The corresponding P(r) distribution. The distribution predicted from the NMR structure (insert in (E)) is shaded gray.
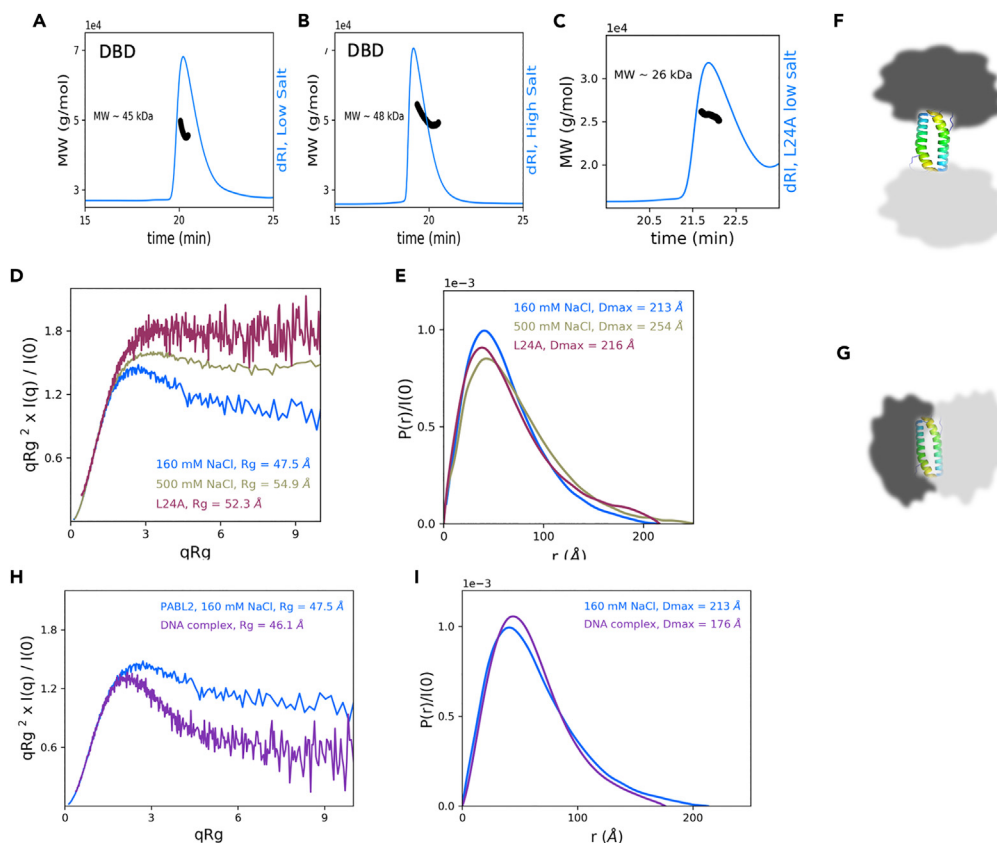
Figure 4. SAXS/MALS analysis of PALB2-DBD

(A–C) SEC elution profile (blue) measured by refractometer and MW estimation by MALS (black) of PALB2-DBD at 160 mM (A) and 500 mM (B) NaCl buffers and of L24A mutant (C) at 160 mM NaCl.

(D) SAXS data for PALB2-DBD at high (green) and low (blue) NaCl concentration buffers and of L24A mutant at 160 mM NaCl (dark red), visualized as a dimensionless Kratky plot. Data were binned logarithmically by factor of 3 for visual clarity.

(E) Pairwise distance distribution functions [$P(r)$] from SAXS measurements of same samples as in (D).

(F and G) Two hypothetical models of IDRs attached to opposite ends of coiled-coil linker. A single domain length in $P(r)$ distribution (E) suggests a compact dimer conformation (bottom).

(H) SAXS data for PALB2-DBD (blue) and complex of PALB2-DBD with dT_{50} (magenta) visualized as a dimensionless Kratky plot. Data were binned logarithmically by factor of 3 for visual clarity. The SAXS profile of the DNA complex is significantly more compact, more closely resembling a scattering for a globular protein than for an IDP.

(I) Pairwise distance distribution functions [$P(r)$] from SAXS measurements of same fragments as in (H).

further complicated by oligomerization (Figures 3E and 3F, data below and ref. 47), we initially evaluate the compaction of monomeric Δ40-DBD using size exclusion chromatography (SEC) to compare the elution time of the protein in a DNA-binding buffer and in the presence of the strong denaturant guanidinium hydrochloride (GdmHCl), which forces RC formation (Figure S3). The protein elutes significantly earlier in 6 M GdmHCl than in non-denaturing DNA-binding buffer. The elution volume under nondenaturing conditions corresponds to a globular protein with a molecular weight only twice that of Δ40-DBD.

Next, we characterized structural organization of the PALB2-DBD dimer using small angle X-ray scattering (SAXS). SAXS can directly measure structural features of proteins in solution and is particularly valuable for IDPs that are not amenable to other structural techniques.[73–75] SAXS measurements were conducted in-line with SEC and multiangle light scattering (MALS) to separate and identify different molecular species. We first analyzed PALB2-DBD in two different buffer conditions with 0.16 M or 0.5 M NaCl (Tables S1 and S2; Figures S4 and S5), followed by studies on the L24A mutant, which does not form dimers at low micromolar concentrations due disrupted hydrophobic core of coiled-coil interface,[47,49,76] and of the PALB2-DBD complex with dT_{50} (Tables S3 and S4; Figures S6–S8). Two salt concentrations were initially used because PALB2-DBD is more soluble and less prone to aggregation in high salt buffer (0.5 M NaCl), whereas DNA binding is strongly inhibited by high salt concentrations.[33] At 0.16 M NaCl PALB2-DBD retains DNA binding activity (Figure S2). MALS measurements unequivocally confirm the dimeric form of PALB2-DBD under both buffer conditions (Figures 4A and 4B) and the monomeric form of L24A mutant at 0.16 M NaCl (Figure 4C). Interestingly, previous measurements of the coiled-coil dimerization constant by NMR revealed K_d = 80 μM for the isolated N-terminal α-helical fragments.[47] Retaining of the dimeric state by PALB2-DBD at lower concentrations even under

nonequilibrium SEC conditions suggests that an interaction between IDRs contributes to the dimer stability together with the coiled-coil interaction.

SAXS analyses resulted in typical IDP scattering patterns, as illustrated by the slow decay of the tail when data are plotted as a dimensionless Kratky plot distribution (Figure 4D). Distribution of PALB2-DBD at 500 mM NaCl appears slightly more compact than a typical disordered IDP, with the slight bell-shaped peak at ~2.5 qR_g and flat tail (Figure 4D, teal). These features are even more pronounced at low salt suggesting an additional compaction at low salt (Figure 4D, blue). Likewise, the estimated values of R_g are 54.9 Å and 47.5 Å for high and low salt conditions, correspondingly. Fitting the 0.5 M NaCl data to a molecular form factor (MFF) fitting protocol developed specifically for IDPs[77,78] yields a Flory exponent ν = 0.52, which describes a polymer dimension dependence on its length ($R_g \sim N^\nu$) (Table S2). This value of ν is slightly lower than those for typical IDPs in good solvent (~0.54–0.55),[77,78] and suggests a relatively compact overall conformation, assuming that this system behaves similarly to a single-chain IDP with a total length of 400 aa due to the almost end-to-end dimerization. In fact, these compaction parameters at 0.5 M NaCl are close to the corresponding values reported for an unstructured PNt domain with smaller single chain size (335 aa).[77] The corresponding values are notably lower in the low salt condition than in the high salt conditions (R_g (47.5 Å) and ν (0.47)), suggesting a role for polar interactions in structure compaction. Interestingly, the distribution obtained for L24A monomer suggests a more disordered state (Figure 4D, dark red) than the dimer under either salt condition. In fact, an estimated R_g value of 52.3 (ν = 0.54) of the monomeric L24A mutant even larger than the R_g of the dimer under same conditions (Figures 4D and 4E), suggesting that the interaction between IDRs subunits leads to compaction of each monomer and of the entire dimer.

Two IDRs in the PALB2-DBD dimer are located at opposite ends of 40 Å-long antiparallel coiled-coil structure and can form two independent or spatially distinct MGs. However, only one dominant length scale is observed in the pairwise distance distribution [$P(r)$] measured in SAXS (Figure 4E) supporting a compact structure (Figure 4G), ruling out the dumbbell model with two distinct MGs (Figure 4F). While the distinction between two models may be less pronounced in case of the disordered structure, the relatively small R_g values from SAXS experiments with the dimer also indicates a compact overall organization.

Compaction of PALB2-DBD upon DNA binding

Following studies on the protein alone, we conducted SEC-MALS-SAXS data on PALB2-DBD with dT_{50} DNA in a low salt buffer with 160 mM NaCl. As this experiment was performed at a different facility (Cornell High Energy Synchrotron Source, CHESS), we also collected control data for PALB2-DBD alone in 160 mM NaCl buffer. The scattering profile for PALB2-DBD alone is in excellent agreement with the previous APS experiment (Figure S9), albeit with slightly larger estimated R_g and $P(r)$ D_{max} values, likely as a result of increased propensity for sample radiation damage at CHESS due to differences in beamline infrastructure.[79] For data collected at CHESS, deconvolution by EFA[80] and/or REGALS[81] was necessary to separate out the component of interest from other species and accumulated radiation damage (Figures S10–S12). Addition of DNA to protein resulted in a significantly more compact structure of the dimer, with a Kratky plot shape more characteristic of a globular protein than an IDP (Figure 4H). Correspondingly, the R_g of the complex with DNA is 46.1 Å, smaller than PALB2-DBD alone under identical experimental conditions (47.5 Å) despite being in complex with DNA. MALS data were highly variable and inconclusive. Analysis of SAXS data yielded an estimated molecular weight of 110 kDa (Table S4), which is very close to molecular weight of PAB2-DBD:dT_{50} complex at 4:1 stoichiometry of 107 kDa. Therefore, SAXS data revealed a tetrameric form of PALB2-DBD complex with ssDNA. Kratky plot and comparable Rg values of the DNA-free dimer and DNA-bound tetramer evidence a significant compactization of the protein within a tetramer.

SAXS-directed modeling of structural ensembles

To obtain further insight into PALB2-DBD structural organization using experimental SAXS results, we performed molecular structure modeling of the protein dimer and of L24A mutant monomer using the program SASSIE[82] (Table S5). An initial pool of structures were generated using the Complex Monte-Carlo algorithm in SASSIE with fixed N-terminal α-helixes and a dimeric coiled-coil interface (aa 11–40) as determined by NMR.[47] The starting model of a dimer was generated by the AlphaFold program using the ColabFold Google server[83] (Figure 3D). The resulting trajectory yielded 34,919 structures, from which a subensemble of structures (selected using GAJOE[74]) provided a good fit ($\chi^2 = 1.01$) to the experimental data of the system in 0.5 M NaCl buffer (Figure 5A). The poll of the best-fit ensemble is bimodal with the majority with lower R_g ~45 Å and a second population with R_g ~62 Å (Figure 5B). Although the experimental Guinier R_g = 54.9 Å is significantly lower than the average R_g ~71 Å of the entire pool of all randomly generated structures, enough compact structures were sampled that the average R_g of the selected ensemble (56.7 Å) is similar to the experimental value.

Fitting data obtained at the low salt concentration (0.16 M NaCl) was more challenging, likely due to the low population of compact structures generated by the unguided SASSIE Monte Carlo simulation. Fitting the low salt condition data using the same structural pool generated for fitting the high salt condition resulted a poorer fit ($\chi^2 = 2.03$, Figure 5C). Guiding the simulation trajectory to an average R_g (the experimental R_g of 47.5 Å) during modeling resulted in an improved fit ($\chi^2 = 1.32$), as simulation was successfully able to generate a structural pool with a much smaller average R_g (visualized in the blue distributions in Figure 5D). A similar bimodal distribution of theoretical R_g for the selected ensemble was obtained even with guided modeling (Figure 5D).

We also performed similar molecular modeling to the L24A SAXS data. An initial ensemble of 38,042 structures was generated using the Monomer Monte Carlo simulation implemented in SASSIE. The starting model used was chain A from the AlphaFold-generated dimer, as described above, with the L24A mutation performed using the simple mutagenesis tool in Pymol. The initial pool of generated structures was relatively well distributed around the experimental R_g (Figure 5F, blue), and a final sub-ensemble (selected using GAJOE[74]) fit the
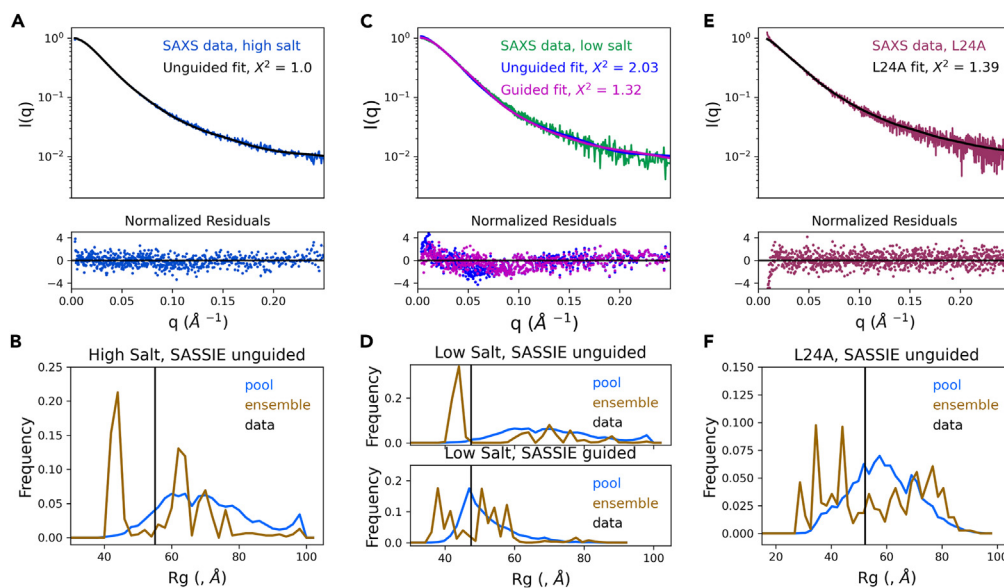
Figure 5. SASSIE fits of experimental SAXS data

(A) Fit of SAXS-derived experimental distance distribution of PALB2-DBD in 500 mM NaCl with theoretical distribution of best fit models calculated from unguided SASSIE models using GAJOE.

(B) R_g distribution of the entire pool of 34,919 structures (blue), experimental R_g (black bar) for 500 mM NaCl data, and distribution of R_g of the best-fit pool structures (brown).

(C and D) similar plots to that of in (A,B) for 160 mM NaCl data with both unguided (blue) and guided (red) fits shown in (C) with corresponding R_g distributions shown in top and bottom panels in (D) for unguided and guided fits, correspondingly.

(E and F) similar fitting and R_g distributions as in (A,B) for data from L24A monomeric mutant in 160 mM NaCl buffer.

experimental data well ($\chi^2 = 1.39$). The distribution of the final ensemble was again somewhat bimodal (Figure 5F, red), though less pronounced than for the dimer.

Single-molecule FRET analysis reveals that PALB2-DBD dynamically condenses DNA

Two studied strand exchange protein families, RecA and Rad52, are characterized by different DNA biding mechanisms. RecA-like recombinases form nucleoprotein filaments stretching out ssDNA.[84–86] Rad52 wraps ssDNA around a toroidal oligomeric structure.[19,20,87] Our previous intensity-based Förster resonance energy transfer (FRET) experiment suggested a Rad52-like mechanism where protein interaction led to increased FRET between Cy3 and Cy5 dyes located at the ends of doubly labeled dT_{40} or dT_{70} oligonucleotides.[33] Titration by PALB2-DBD led to higher FRET efficiency, thus resembling the results of a similar experiment with Rad52.[87] However, these measurements were performed on an ensemble averaged in a fluorimeter, so the molecular species and sequence of events that generated the result could not be precisely identified, particularly considering the disordered nature of PALB2-DBD and oligomerization.

To address the limitation of our previous studies, we performed comparable experiments utilizing single-molecule FRET (smFRET). We used a confocal setup to determine the FRET efficiency of freely diffusing single DNA molecules labeled with the FRET pair Cy3/Cy5 in the absence and presence of PALB2-DBD. We used Pulsed interleaved excitation (PIE) to calculate the stoichiometry for each molecule, as the PIE value enables the identification of molecules containing the correct 1:1 ratio of donor and acceptor (Figure 6A) and the detection of other photophysical phenomena such as bleaching, blinking, and protein-induced fluorescent enhancement (PIFE).[88–91] Measurements were performed with several ssDNA substrates with fluorescent dyes placed at different distances: dT_{50} with Cy3 at the 5′ end and Cy5 at positions 25 or 50, and dT_{70} labeled at the 5′ and 3′ ends. Cy3-dT_{70}-Cy5 and Cy3-dT_{50}-Cy5 substrates in solution show a single, symmetric distribution with mean FRET of 0.11 (Figure 6A) and 0.18 (Figure 6B), respectively, in agreement with published results.[92] The addition of PALB2-DBD significantly increased mean FRET, thereby confirming observations from our previous studies.[33] Two distinct FRET populations were observed in the presence of PALB2, corresponding to two different states of DNA bound to the protein, one significantly more condensed than the other with mean FRET of 0.34 and 0.71 in case of Cy3-dT_{70}-Cy5 (Figure 6A, the gray panel above each 2D plot). The mean FRET value for each peak is invariant for a given DNA fragment, whereas the population of each state changes upon titration by PALB2-DBD. A medium FRET state of Cy3-dT_{70}-Cy5 is a predominant species at 1 μM PALB2-DBD, whereas high FRET is a major peak at 3 μM PALB2-DBD (Figure 6A). Titration of dT_{50} by PALB2-DBD (Figure 5B) revealed similar distributions of two populations of invariant mean FRET peaks of 0.45 and 0.79, with a high FRET peak becoming more predominant at high protein concentration. These results suggest that PALB2-DBD binds to multiple sites within the same DNA strand, thereby dynamically controlling its conformation. They also suggest that the PALB2-DBD concentration is an important factor in controlling DNA conformation.
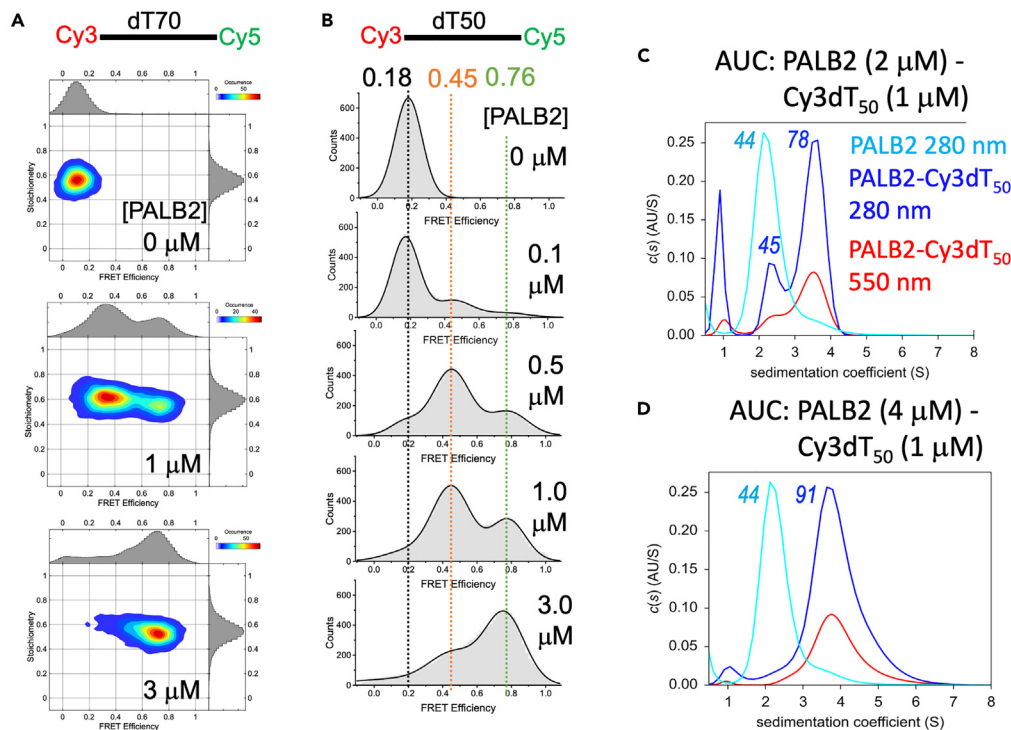
Figure 6. Bimodal DNA compaction revealed by confocal smFRET and two oligomeric states revealed by AUC

(A) 2D plots of FRET efficiency versus stoichiometry for 100 pM Cy3-dT$_{70}$-Cy5 alone (top panel) and in the presence of 1.0 μM (middle panel) and 3.0 μM PALB2-DBD (bottom panel) in a buffer with 160 mM NaCl, 20 mM HEPES pH 7.5, 1 mM TCEP. FRET efficiency histograms are shown in gray above each plot and FRET pair stoichiometry in gray on the right side of each plot.

(B) FRET histograms (gray) of 100 pM Cy3-dT$_{50}$-Cy5 titrated by PALB2-DBD. Black lines show fitting of data using three species as Gaussian distributions. Protein concentrations are shown on each graph. Mean FRET values of major peaks are shown with color corresponding to each peak.

(C) Sedimentation coefficient distribution of PALB2-DBD at 6 μM (cyan), of PALB2-DBD at 2 μM in the presence of 1 μM Cy3-dT$_{50}$ (blue, red) measured at absorption wavelengths of 280 nm (blue) and at 550 nm (red) in identical buffer to that of in (A, B).

(D) Similar distributions as in (C) but at 4 μM PALB2-DBD mixed with 1 μM Cy3-dT$_{50}$.

A similar trend was observed for a dT$_{50}$ substrate with Cy3 and Cy5 labels placed 25 nucleotides apart (Figure S13A). Mean FRET for free DNA is 0.45, the major peak at 1 μM PALB2-DBD is at FRET of 0.71, and the peak for 3 μM PALB2-DBD is at FRET of 0.89. DNA compaction is significant for this substrate as well, although it is challenging to deconvolute two separate peaks at each protein concentration due to the initially high FRET for free DNA. A similar trend of DNA compaction proportional to the number of nucleotides between labels is observed for all three cases. For example, changes in FRET between the peak of free DNA and the first peak of DNA in complex with PALB2-DBD for distances of 70, 50, and 25 nucleotides were from 0.11 to 0.34, from 0.18 to 0.45, and from 0.45 to 0.71, respectively. These results combined with a disordered protein structure makes unlikely a Rad52-like wrapping model of DNA binding, in which the FRET change between remote ends is greater than that between labels situated closer in the nucleotide sequence. It suggests a random coil model of ssDNA conformation, in which the average distance between ends is restricted due to interactions with two major DNA-binding sites in a compact PALB2-DBD dimer. In this model, two random parts of ssDNA interact with two DNA-binding sites situated within an average R_g distance from each other (Figure 7). This model explains an invariant position of the peak with an intermediate mean FRET. The mechanism of an additional DNA compaction corresponding to a high FRET peak is likely connected with protein tetramerization observed in SAXS. To evaluate the role of PALB2-DBD oligomerization in DNA compaction, we tested a Δ40-DBD variant lacking the coiled-coil dimerization interface using Cy3-dT$_{50}$-Cy5 (Figure S13B). DNA compaction also was observed in this case, albeit at higher protein concentrations, reflecting a significantly reduced DNA binding affinity.[33] There was a fraction of free DNA in solution even at 10 μM protein. FRET distributions were significantly broader and more heterogeneous corresponding to multiple species of DNA conformations. The lack of two distinct peaks in the case of Δ40-DBD indirectly supports oligomerization-dependent DNA compaction. In this case, the Δ40-DBD will form oligomers by addition of a single monomer (dimers, trimers, tetramers) resulting in a broad distribution of DNA conformations, while PALB2-DBD forms dimers and tetramers or dimer of dimers resulting in two distinct FRET values.

The tetramerization hypothesis is supported by a previously observed 1:4 stoichiometry of DNA binding in fluorescence polarization and ensemble FRET assays[33] and SEC/MALS/SAXS experiments, described above, conducted at relatively high protein concentration. To further investigate oligomeric states of the protein at different concentrations in the presence of ssDNA under equilibrium conditions, we conducted
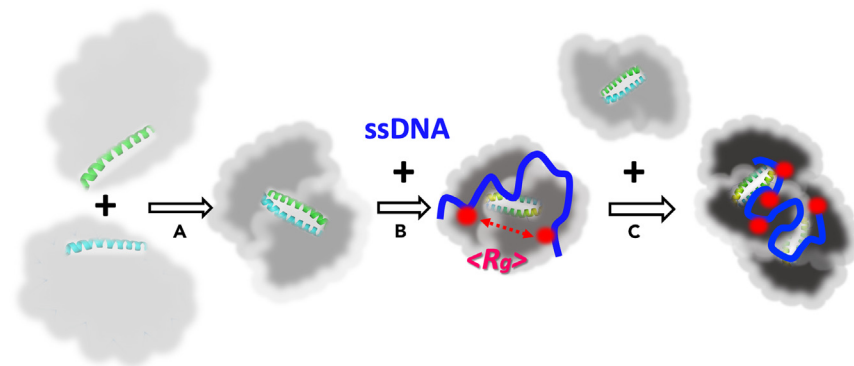
Figure 7. Model of oligomerization-dependent compaction of PALB2-DBD and of ssDNA compaction by PALB2-DBD dimer and tetramer

(A) PALB2-DBD dimerization is mediated by coiled-coil and IDR-IDR interactions leading to compaction of the structure.

(B) ssDNA (blue) binds to PALB2-DBD dimer in a random but a significantly more compact conformation, comparatively to its free state in solution, due to interaction with two major DNA-binding sites (red circles) situated at an average distance of R_g from each other. Interaction with ssDNA leads to an additional compaction of PALB2-DBD dimer.

(C) Higher concentration of PALB2-DBD leads to tetramerization and additional compaction of ssDNA bound to tetramers and the compaction of the protein itself.

sedimentation velocity experiments with PALB2-DBD under identical conditions in the presence of Cy3-dT$_{50}$ (Figures 6C and 6D). DNA was labeled with Cy3 to distinguish its position from that of protein-only. Measurements were repeated at two different protein concentrations corresponding to DNA:protein molar ratios of 1:2 and 1:4 with DNA at 1 μM concentration in both experiments. PALB2-DBD alone sediments at molecular weight of ∼45 kDa corresponding to a dimer (cyan). Three peaks were observed upon addition of ssDNA at 1:2 DNA:protein ratio, one at low molecular weight position, corresponding to free DNA, the second at position of PALB2-DBD dimer (an apparent MW = 45.2 kDa), and the third at position with molecular weight of ∼78 kDa, corresponding to the tetramer. A low apparent molecular weight (theoretical value is 92 kDa) of this peak is likely due to the dynamic exchange between different oligomeric states. All three peaks are present in absorption profile at 550 nm, corresponding to maximum absorption of Cy3, confirming that Cy3-dT$_{50}$ is bound to dimers and tetramers. Only one, albeit wider peak corresponding to the tetramer is present at 1:4 protein ratio with a calculated molecular weight of 91 kDa. Importantly, tetramers were also observed in the AUC experiment with twice shorted dT$_{22}$ substrate (Figure S14) ruling out independent binding of two dimers to a long ssDNA. Thus, SAXS, AUC and smFRET data revealed a ssDNA- and protein-concentration dependent oligomerization of PALB2-DBD with a strong protein structure compaction as well as ssDNA compaction.

DISCUSSION

Our data indicate that PALB2-DBD is an intrinsically disordered domain that forms a dimer stabilized by both a coiled-coil interface between N-terminal α-helices and the interactions between IDRs. Although PALB2-DBD is comprised of a low complexity sequence, it was unexpected that an unstructured protein can support an elaborate multisubstrate and multistep strand exchange. Results render novel structural and DNA interaction properties of PALB2-DBD which have not been described for any other characterized DNA binding domains, to our knowledge. While the mechanism of strand exchange remains to be investigated, results clearly suggest a completely different mechanism from that of RecA-like recombinases and Rad52.

SEC and SAXS results revealed that the PALB2-DBD dimer has a compact structure not typical for scaffold structures interacting with multiple proteins. Note, that this fragment includes several distinct protein binding sites for interactions with BRCA1, RAD51 and KEAP1.[35] The compaction is achieved through favored intermolecular and intramolecular interactions between two IDRs as the monomeric mutant L24A is significantly less compact than the dimer. The Flory scaling exponent describing a polymer dimension dependence on its length (ν) is around 0.5, which is expected for a non-self-avoiding random coil and corresponds to a Θ solvent where intermolecular and solvent interactions counterbalance each other.[78] A noticeable reduction of R_g and ν in a low salt buffer suggests contribution of polar intermolecular interactions to the compaction. A similar salt effect on IDR structures due to charge screening at physiological salt concentrations were reported for other proteins.[93] The interaction between two IDRs is weak, since Δ40-DBD and L24A are monomeric in solution at micromolar concentrations in the absence of ssDNA. However, PALB2-DBD dimer is apparently more stable than that of isolated coiled-coil helixes. A single dominant length scale observed in the pairwise distance distribution [P(r)] measured in SAXS (Figures 4E and 4I) further supports interactions between entire domains and not only coiled-coil helixes. Importantly, IDRs are more compact within the dimer than in a monomeric state as evidenced by comparable R$_g$ of the dimer and monomer. Therefore, a simple proximity of two monomers with identical sequences leads to significant compaction of disordered structural ensembles which they form. It is tempting to hypothesize that similar interaction between IDRs of other proteins can contribute to heterooligomerization within DNA repair complexes. For example, PALB2 binds BRCA1 through the same N-terminal α-helix that forms a coiled-coil interface with the BRCA1 α-helix[50,76] surrounded IDRs.[94–96] This interaction can be strengthened by attractions between IDRs of two proteins. SAXS data demonstrated that ssDNA binding leads to tetramerization with an additional compaction

of the IDRs and the entire oligomeric structure. Tetramerization is driven by interactions between IDRs due to altered conformations of structural ensembles in the presence of ssDNA. This result is unexpected as ssDNA should screen positive charges stimulating repulsion between negatively charged amino acids. Interestingly, a 2-fold structural compaction of ssDNA-bound tetramer versus DNA-free dimer did not result in a reduced local flexibility of tested peptide regions of PALB2-DBD (Figure 3), except of the main DNA-binding site. The mechanism of oligomerization- and DNA interaction-induced protein compaction has to be further investigated through computational modeling and mutagenesis studies.

Strong compaction of ssDNA bound to PALB2-DBD rules out a RecA-like mechanism, where sDNA is stretched out.[97] In case of Rad52, ssDNA wraps around the toroidal oligomer backbone, bringing distant ends of DNA in close proximity.[87,98] However, the wrapping model does not fit behavior ssDNA bound to PALB2 and is unlikely for the disordered DNA binding domain. Thus, the mechanism of PALB2-DBD interaction with ssDNA differs from those of RecA and Rad52.

The mechanism behind strongly compacted ssDNA bound to tetramer is less clear. Such compaction of DNA bound to a larger complex can be achieved by condensation of DNA-binding sites around a ssDNA molecule.

The physiological role of PALB2-DBD tetramerization remains unclear considering the required stoichiometric excess or relatively high concentration of protein, which may not be achieved for a full-length protein and/or its functional complexes with even larger BRCA2 and BRCA1. However, attractions between IDRs can stimulate formation of heterooligomeric complexes with disordered parts of BRCA1/BRCA2 and other protein partners or the formation of DNA-repair condensates through liquid-liquid phase separation (LLPS). The probability of forming a droplet state through LLPS (p_{LLPS}) for PALB2-DBD and PALB2 is very high, as calculated using FuzDrop analysis (0.9622 and 0.9412, respectively, Figures S15A and S15B). Since these values significantly exceed the 0.6 threshold, both PALB2-DBD and PALB2 are considered as potential droplet-drivers.[62] Therefore, the observed limited oligomerization of PALB2-DBD and multivalent interactions (coiled-coil, IDR-IDR, protein-DNA) may reflect its ability to stimulate formation of condensed phase under certain conditions. Indeed, in preliminary experiments we observed an increase in solution turbulence upon salt concentration decrease (Figure S15C). The effect is enhanced in the presence of ssDNA and is completely reversable upon salt increase. Visual inspection of turbid solutions reveals formation of 2–6 μm droplets (Figures S15D and S15E). While a comprehensive characterization of liquid properties of the observed droplets and their function requires additional experiment, these preliminary observations further support the predicted phase separation properties of PALB2-DBD. BRCA1, PALB2 and BRCA2 have not been directly observed in condensates, however, several interacting partners were reported to stimulate the formations of condensates in cells including RNF168[99–101] and RAP80,[102] where phase separation properties of RAP80 correlate with BRCA1 recruitment to DSB. Furthermore, PALB2 resides at transcription regulation complexes[103–107] reported to form transcription activation or repression condensates.[108]

Previously reported strand annealing and strand exchange properties of PALB2-DBD combined with a dynamic nature of its structure and DNA interaction suggest a potential chaperone-like mechanism where transient iterative interactions can promote strand separation and re-annealing. Chaperon activities are critical for RNA metabolism due to the complexity, diversity, and the dynamic nature of RNA structures and their complexes. Various mechanisms are supported by a wide spectrum of proteins ranging from ATP-dependent helicases to small IDPs.[109,110] *Escherichia coli* StpA protein promotes RNA strand annealing and strand displacement,[111] similar to those reported for PALB2-DBD.[33] SptA is a small globular protein that forms dimers required for these activities. Other examples include the structured globular FANCA protein of the Fanconi anemia (FA) complex[29] and limited reports of D loop formation by FET proteins critical for RNA metabolism, specifically pro-oncoprotein TLS/FUS and the human splicing factor PSF/hPOMp100.[30–32] The latter proteins include structured domains (RNA recognition motif RRM and zinc finger), sequences of low complexity, and prion-like RGG domains implicated in higher-order self-assemblies. There are examples of disordered RNA chaperones composed of positively charged peptides that promote the formation of compact nucleic acid conformations by acting as polypeptide counterions to overcome repulsive electrostatic interactions of RNA or DNA chains.[44–46] The mechanism of DNA compaction by PALB2 differs from such model as PALB2-DBD has overall neutral charge and significant hydrophobicity. Chaperone activities are not implicated in DNA metabolism due to restricted conformational space of DNA helix and a large size of chromosomal fragments. However, multiple DNA metabolism processes (e.g., repair of replication forks collided with transcription complexes and replication fork reversal) require the formation of transient multichain DNA and RNA-DNA structures and other higher-order nucleic acid interactions[112–114] that may benefit from strand exchange activity of PALB2-DBD or of similar unstructured domains of DNA-repair proteins. The fact that PALB2 resides at the promoter regions of highly transcribed genes under nondamaging conditions[107] further supports this functional hypothesis.

DNA-binding proteins are enriched in disordered domains/regions, have higher disordered content in eukaryotes,[115] and many IDRs coincide with DNA-binding domains.[94] Such regions may simply increase the chromatin affinity by transient DNA binding without forming a strong roadblock on DNA, except in cases of structure-specific interactions like nucleolin-G–quadruplex recognition.[116] It is tempting to suggest that DNA-binding IDRs may have evolved to perform more complex reactions, such as a described strand exchange or DNA chaperon activities, using an evolutionarily inexpensive functional unit that facilitates formation and resolution of transient multichain DNA/RNA intermediates. Although this proposed reaction is more complex than others reported for IDRs, it depends on simple structural requirements and similar IDRs can be incorporated into larger proteins (e.g., DNA-binding regions in scaffold BRCA1[94–96] and BRCA2[117,118]). Analysis of DNA-binding domain of BRCA1 show rather impressive overall similarity to sequence properties of PALB2-DBD (Figure S16) providing support to the validity of this hypothesis. These disordered domains can function synergistically with RAD51,[33,41,119] or they can independently perform a required reaction without forming stable presynaptic RAD51 filaments. Furthermore, such IDRs often have high propensity for phase separation, suggesting that they can stimulate formation of DNA repair condensates and function within such condensates. For example,

sequence analysis of BRCA1 DBD region in vicinity of PALB2-binding site revealed a high probability of droplet formation by this region (Figure S16E). This is a very compelling possibility, as the LLPS-driven formation of various membrane-less organelles (MLOs) and biomolecular condensates is considered now as one of the crucial organizing principles of the intracellular space responsible for regulation and control of numerous cellular processes.[120] Those include DNA repair foci formed upon DNA damage response[121–125]; chromatin-associated promyelocytic leukemia Nuclear Bodies[126]; liquid condensates on DNA/RNA matrices containing related proteins and G-quadruplexes (G4s) and responsible for reparation, transcription, genome integrity maintenance, and chromatin remodeling[127]; nuclear condensates containing polycomb group (PcG) proteins that contribute to the reshaping of chromatin architecture[128]; and intrinsic chromatin condensates related to various chromatin-centric processes, such as transcription, loop extrusion, and remodeling[129] to name a few. Therefore, it is likely that the LLPS-driven formation of biomolecular condensates can play a role in complex functionality of PALB2-DBD and similar regions of other DNA-binding IDRs.

Limitations of the study

All structural and biochemical characterizations were performed with isolated domain of PALB2. Additional studies are required to investigate the role of the discovered properties for the function of the full-length PALB2 and its complexes with interacting partners. Additional experiments are required for the insight into novel strand exchange mechanism.

RESOURCE AVAILABILITY

Lead contact

Further information and requests for resources and reagents should be directed to and will be fulfilled by the lead contact, S.K. (sergey.korolev@health.slu.edu).

Material availability

All protein expression plasmids are freely available on request.

Data and code availability

- SAXS scattering data are deposited to SASBDB (https://www.sasbdb.org/) with accession IDs: SASDBD:SASDVQ7 for L24A mutant, SASDBD:SASDSZ5 for dimer at 0.5M NaCl, ID SASDBD:SASDS26 for dimer at 0.16M NaCl, and SASDBD:SASDVR7 for complex with DNA. SASSIE Monte Carlo structural ensembles for unguided and guided dimers and for L24A monomer are deposited at Zendo with https://doi.org/10.5281/zenodo.13892101.
- No new code is developed in this study.
- The smFRET data in PTU file format (time-correlated single-photon counting data) are available on request.

AUTHOR CONTRIBUTIONS

S.K. conceptualized the study; Y.K., M.B.W., J.M.R., N.C., A.G., R.D., J.H., and N.P.; SK designed, performed, and analyzed experiments; M.B.W. performed computational modeling of SAXS data; R.D. designed and analyzed cwEPR; N.C. and A.G. measured turbulence and droplet formation; V.N.U. performed sequence analysis; N.P. helped to design and analyze confocal smFRET; S.K. wrote the manuscript with input from all authors, supervised the study, and acquired funding.

DECLARATION OF INTERESTS

None.

STAR★METHODS

Detailed methods are provided in the online version of this paper and include the following:

- KEY RESOURCES TABLE
- METHOD DETAILS
  - Cloning and purification
  - Circular dichroism (CD)
  - Electron paramagnetic resonance (EPR) analysis
  - SEC-MALS-SAXS analysis
  - Confocal smFRET analysis
  - Analytical ultracentrifugation (AUC)
  - Turbidity and droplets formation
- QUANTIFICATION AND STATISTICAL ANALYSIS

SUPPLEMENTAL INFORMATION

Supplemental information can be found online at https://doi.org/10.1016/j.isci.2024.111259.

REFERENCES

1. Cox, M.M. (1999). Recombinational DNA repair in bacteria and the RecA protein. Prog. Nucleic Acid Res. Mol. Biol. *63*, 311–366.

2. Cox, M.M. (2001). Historical overview: searching for replication help in all of the rec places. Proc. Natl. Acad. Sci. USA *98*, 8173–8180. https://doi.org/10.1073/pnas.131004998/15/8173.

3. San Filippo, J., Sung, P., and Klein, H. (2008). Mechanism of eukaryotic homologous recombination. Annu. Rev. Biochem. *77*, 229–257. https://doi.org/10.1146/annurev.biochem.77.061306.125255.

4. Krogh, B.O., and Symington, L.S. (2004). Recombination proteins in yeast. Annu. Rev. Genet. *38*, 233–271. https://doi.org/10.1146/annurev.genet.38.072902.091500.

5. Kowalczykowski, S.C. (2015). An Overview of the Molecular Mechanisms of Recombinational DNA Repair. Cold Spring Harb. Perspect. Biol. *7*, a016410. https://doi.org/10.1101/cshperspect.a016410.

6. Roca, A.I., and Cox, M.M. (1990). The RecA protein: structure and function. Crit. Rev. Biochem. Mol. Biol. *25*, 415–456. https://doi.org/10.3109/10409239009090617.

7. Cox, M.M. (2003). The bacterial RecA protein as a motor protein. Annu. Rev. Microbiol. *57*, 551–577. https://doi.org/10.1146/annurev.micro.57.030502.090953.

8. Morrical, S.W. (2015). DNA-pairing and annealing processes in homologous recombination and homology-directed repair. Cold Spring Harb. Perspect. Biol. *7*, a016444. https://doi.org/10.1101/cshperspect.a016444.

9. Sung, P., and Klein, H. (2006). Mechanism of homologous recombination: mediators and helicases take on regulatory functions. Nat. Rev. Mol. Cell Biol. *7*, 739–750. https://doi.org/10.1038/nrm2008.

10. Liu, J., and Heyer, W.D. (2011). Who's who in human recombination: BRCA2 and RAD52. Proc. Natl. Acad. Sci. USA *108*, 441–442. https://doi.org/10.1073/pnas.1016614108.

11. Symington, L.S. (2002). Role of RAD52 epistasis group genes in homologous recombination and double-strand break repair. Microbiol. Mol. Biol. Rev. *66*, 630–670.

12. Cox, M.M. (2007). Regulation of bacterial RecA protein function. Crit. Rev. Biochem. Mol. Biol. *42*, 41–63.

13. Beernink, H.T., and Morrical, S.W. (1999). RMPs: recombination/replication mediator proteins. Trends Biochem. Sci. *24*, 385–389.

14. Mazina, O.M., Keskin, H., Hanamshet, K., Storici, F., and Mazin, A.V. (2017). Rad52 Inverse Strand Exchange Drives RNA-Templated DNA Double-Strand Break Repair. Mol. Cell *67*, 19–29.e3. https://doi.org/10.1016/j.molcel.2017.05.019.

15. Lee, M., Lee, C.H., Demin, A.A., Munashingha, P.R., Amangyeld, T., Kwon, B., Formosa, T., and Seo, Y.S. (2014). Rad52/Rad59-dependent recombination as a means to rectify faulty Okazaki fragment processing. J. Biol. Chem. *289*, 15064–15079. https://doi.org/10.1074/jbc.M114.548388.

16. Bi, B., Rybalchenko, N., Golub, E.I., and Radding, C.M. (2004). Human and yeast Rad51 proteins promote DNA strand exchange. Proc. Natl. Acad. Sci. USA *101*, 9568–9572. https://doi.org/10.1073/pnas.0403205101.

17. Mortensen, U.H., Lisby, M., and Rothstein, R. (2009). Rad52. Curr. Biol. *19*, R676–R677. https://doi.org/10.1016/j.cub.2009.06.001.

18. Sung, P. (1997). Function of yeast Rad52 protein as a mediator between replication protein A and the Rad51 recombinase. J. Biol. Chem. *272*, 28194–28197.

19. Saotome, M., Saito, K., Yasuda, T., Ohtomo, H., Sugiyama, S., Nishimura, Y., Kurumizaka, H., and Kagawa, W. (2018). Structural Basis of Homology-Directed DNA Repair Mediated by RAD52. iScience *3*, 50–62. https://doi.org/10.1016/j.isci.2018.04.005.

20. Singleton, M.R., Wentzell, L.M., Liu, Y., West, S.C., and Wigley, D.B. (2002). Structure of the single-strand annealing domain of human RAD52 protein. Proc. Natl. Acad. Sci. USA *99*, 13492–13497.

21. Kagawa, W., Kurumizaka, H., Ishitani, R., Fukai, S., Nureki, O., Shibata, T., and Yokoyama, S. (2002). Crystal structure of the homologous-pairing domain from the human Rad52 recombinase in the undecameric form. Mol. Cell *10*, 359–371.

22. Yasuhara, T., Kato, R., Hagiwara, Y., Shiotani, B., Yamauchi, M., Nakada, S., Shibata, A., and Miyagawa, K. (2018). Human Rad52 Promotes XPG-Mediated R-loop Processing to Initiate Transcription-Associated Homologous Recombination Repair. Cell *175*, 558–570.e11. https://doi.org/10.1016/j.cell.2018.08.056.

23. Hall, S.D., and Kolodner, R.D. (1994). Homologous pairing and strand exchange promoted by the Escherichia coli RecT protein. Proc. Natl. Acad. Sci. USA *91*, 3205–3209. https://doi.org/10.1073/pnas.91.8.3205.

24. Murphy, K.C. (2012). Phage recombinases and their applications. Adv. Virus Res. *83*, 367–414. https://doi.org/10.1016/B978-0-12-394438-2.00008-6.

25. Reuven, N.B., Staire, A.E., Myers, R.S., and Weller, S.K. (2003). The herpes simplex virus type 1 alkaline nuclease and single-stranded DNA binding protein mediate strand exchange in vitro. J. Virol. *77*, 7425–7433. https://doi.org/10.1128/jvi.77.13.7425-7433.2003.

26. Fitschen, L.J., Newing, T.P., Johnston, N.P., Bell, C.E., and Tolun, G. (2024). Half a century after their discovery: Structural insights into exonuclease and annealase proteins catalyzing recombineering. Eng. Microbiol. *4*, 100120–103703.

27. Passy, S.I., Yu, X., Li, Z., Radding, C.M., and Egelman, E.H. (1999). Rings and filaments of beta protein from bacteriophage lambda suggest a superfamily of recombination proteins. Proc. Natl. Acad. Sci. USA *96*, 4279–4284. https://doi.org/10.1073/pnas.96.8.4279.

28. Zhang, J., Xing, X., Herr, A.B., and Bell, C.E. (2009). Crystal structure of E. coli RecE protein reveals a toroidal tetramer for processing double-stranded DNA breaks. Structure *17*, 690–702. https://doi.org/10.1016/j.str.2009.03.008.

29. Benitez, A., Liu, W., Palovcak, A., Wang, G., Moon, J., An, K., Kim, A., Zheng, K., Zhang, Y., Bai, F., et al. (2018). FANCA Promotes DNA Double-Strand Break Repair by Catalyzing Single-Strand Annealing and Strand Exchange. Mol. Cell *71*, 621–628.e4. https://doi.org/10.1016/j.molcel.2018.06.030.

30. Baechtold, H., Kuroda, M., Sok, J., Ron, D., Lopez, B.S., and Akhmedov, A.T. (1999). Human 75-kDa DNA-pairing protein is identical to the pro-oncoprotein TLS/FUS

and is able to promote D-loop formation. J. Biol. Chem. *274*, 34337–34342. https://doi.org/10.1074/jbc.274.48.34337.

31. Schwartz, J.C., Cech, T.R., and Parker, R.R. (2015). Biochemical Properties and Biological Functions of FET Proteins. Annu. Rev. Biochem. *84*, 355–379. https://doi.org/10.1146/annurev-biochem-060614-034325.

32. Akhmedov, A.T., and Lopez, B.S. (2000). Human 100-kDa homologous DNA-pairing protein is the splicing factor PSF and promotes DNA strand invasion. Nucleic Acids Res. *28*, 3022–3030. https://doi.org/10.1093/nar/28.16.3022.

33. Deveryshetty, J., Peterlini, T., Ryzhikov, M., Brahiti, N., Dellaire, G., Masson, J.Y., and Korolev, S. (2019). Novel RNA and DNA strand exchange activity of the PALB2 DNA binding domain and its critical role for DNA repair in cells. Elife *8*, e44063. https://doi.org/10.7554/eLife.44063.

34. Xia, B., Sheng, Q., Nakanishi, K., Ohashi, A., Wu, J., Christ, N., Liu, X., Jasin, M., Couch, F.J., and Livingston, D.M. (2006). Control of BRCA2 cellular and clinical functions by a nuclear partner, PALB2. Mol. Cell *22*, 719–729. https://doi.org/10.1016/j.molcel.2006.05.022.

35. Ducy, M., Sesma-Sanz, L., Guitton-Sert, L., Lashgari, A., Gao, Y., Brahiti, N., Rodrigue, A., Margaillan, G., Caron, M.C., Côté, J., et al. (2019). The Tumor Suppressor PALB2: Inside Out. Trends Biochem. Sci. *44*, 226–240. https://doi.org/10.1016/j.tibs.2018.10.008.

36. Venkitaraman, A.R. (2014). Cancer suppression by the chromosome custodians, BRCA1 and BRCA2. Science *343*, 1470–1475. https://doi.org/10.1126/science.1252230.

37. Sharan, S.K., Morimatsu, M., Albrecht, U., Lim, D.S., Regel, E., Dinh, C., Sands, A., Eichele, G., Hasty, P., and Bradley, A. (1997). Embryonic lethality and radiation hypersensitivity mediated by Rad51 in mice lacking Brca2. Nature *386*, 804–810.

38. Moynahan, M.E., Pierce, A.J., and Jasin, M. (2001). BRCA2 is required for homology-directed repair of chromosomal breaks. Mol. Cell *7*, 263–272.

39. Davies, A.A., Masson, J.Y., McIlwraith, M.J., Stasiak, A.Z., Stasiak, A., Venkitaraman, A.R., and West, S.C. (2001). Role of BRCA2 in control of the RAD51 recombination and DNA repair protein. Mol. Cell *7*, 273–282.

40. Venkitaraman, A.R. (2000). The breast cancer susceptibility gene, BRCA2: at the crossroads between DNA replication and recombination? Philos. Trans. R. Soc. Lond. B Biol. Sci. *355*, 191–198.

41. Buisson, R., Dion-Côté, A.M., Coulombe, Y., Launay, H., Cai, H., Stasiak, A.Z., Stasiak, A., Xia, B., and Masson, J.Y. (2010). Cooperation of breast cancer proteins PALB2 and piccolo BRCA2 in stimulating homologous recombination. Nat. Struct. Mol. Biol. *17*, 1247–1254. https://doi.org/10.1038/nsmb.1915.

42. Dray, E., Etchin, J., Wiese, C., Saro, D., Williams, G.J., Hammel, M., Yu, X., Galkin, V.E., Liu, D., Tsai, M.S., et al. (2010). Enhancement of RAD51 recombinase activity by the tumor suppressor PALB2. Nat. Struct. Mol. Biol. *17*, 1255–1259. https://doi.org/10.1038/nsmb.1916.

43. van der Lee, R., Buljan, M., Lang, B., Weatheritt, R.J., Daughdrill, G.W., Dunker, A.K., Fuxreiter, M., Gough, J., Gsponer, J., Jones, D.T., et al. (2014). Classification of intrinsically disordered regions and proteins. Chem. Rev. *114*, 6589–6631. https://doi.org/10.1021/cr400525m.

44. Holmstrom, E.D., Liu, Z., Nettels, D., Best, R.B., and Schuler, B. (2019). Disordered RNA chaperones can enhance nucleic acid folding via local charge screening. Nat. Commun. *10*, 2453. https://doi.org/10.1038/s41467-019-10356-0.

45. Vo, M.N., Barany, G., Rouzina, I., and Musier-Forsyth, K. (2009). HIV-1 nucleocapsid protein switches the pathway of transactivation response element RNA/DNA annealing from loop-loop "kissing" to "zipper. J. Mol. Biol. *386*, 789–801. https://doi.org/10.1016/j.jmb.2008.12.070.

46. Koculi, E., Thirumalai, D., and Woodson, S.A. (2006). Counterion charge density determines the position and plasticity of RNA folding transition states. J. Mol. Biol. *359*, 446–454. https://doi.org/10.1016/j.jmb.2006.03.031.

47. Song, F., Li, M., Liu, G., Swapna, G.V.T., Daigham, N.S., Xia, B., Montelione, G.T., and Bunting, S.F. (2018). Antiparallel Coiled-Coil Interactions Mediate the Homodimerization of the DNA Damage-Repair Protein PALB2. Biochemistry *57*, 6581–6591. https://doi.org/10.1021/acs.biochem.8b00789.

48. Sy, S.M.H., Huen, M.S.Y., and Chen, J. (2009). PALB2 is an integral component of the BRCA complex required for homologous recombination repair. Proc. Natl. Acad. Sci. USA *106*, 7155–7160. https://doi.org/10.1073/pnas.0811159106.

49. Buisson, R., and Masson, J.Y. (2012). PALB2 self-interaction controls homologous recombination. Nucleic Acids Res. *40*, 10312–10323. https://doi.org/10.1093/nar/gks807.

50. Zhang, F., Ma, J., Wu, J., Ye, L., Cai, H., Xia, B., and Yu, X. (2009). PALB2 links BRCA1 and BRCA2 in the DNA-damage response. Curr. Biol. *19*, 524–529. https://doi.org/10.1016/j.cub.2009.02.018.

51. Piovesan, D., Del Conte, A., Clementel, D., Monzon, A.M., Bevilacqua, M., Aspromonte, M.C., Iserte, J.A., Orti, F.E., Marino-Buslje, C., and Tosatto, S.C.E. (2023). MobiDB: 10 years of intrinsically disordered proteins. Nucleic Acids Res. *51*, D438–D444. https://doi.org/10.1093/nar/gkac1065.

52. Jumper, J., Evans, R., Pritzel, A., Green, T., Figurnov, M., Ronneberger, O., Tunyasuvunakool, K., Bates, R., Žídek, A., Potapenko, A., et al. (2021). Highly accurate protein structure prediction with AlphaFold. Nature *596*, 583–589. https://doi.org/10.1038/s41586-021-03819-2.

53. Uversky, V.N. (2002). Natively unfolded proteins: a point where biology waits for physics. Protein Sci. *11*, 739–756. https://doi.org/10.1110/ps.4210102.

54. Uversky, V.N., Gillespie, J.R., and Fink, A.L. (2000). Why are "natively unfolded" proteins unstructured under physiologic conditions? Proteins *41*, 415–427. https://doi.org/10.1002/1097-0134(20001115)41:3<415::aid-prot130>3.0.co;2-7.

55. Holehouse, A.S., Das, R.K., Ahad, J.N., Richardson, M.O.G., and Pappu, R.V. (2017). CIDER: Resources to Analyze Sequence-Ensemble Relationships of Intrinsically Disordered Proteins. Biophys. J. *112*, 16–21. https://doi.org/10.1016/j.bpj.2016.11.3200.

56. Xue, B., Dunbrack, R.L., Williams, R.W., Dunker, A.K., and Uversky, V.N. (2010). PONDR-FIT: a meta-predictor of intrinsically disordered amino acids. Biochim. Biophys. Acta *1804*, 996–1010. https://doi.org/10.1016/j.bbapap.2010.01.011.

57. Peng, K., Radivojac, P., Vucetic, S., Dunker, A.K., and Obradovic, Z. (2006). Length-dependent prediction of protein intrinsic disorder. BMC Bioinf. *7*, 208. https://doi.org/10.1186/1471-2105-7-208.

58. Dosztányi, Z., Csizmok, V., Tompa, P., and Simon, I. (2005). The pairwise energy content estimated from amino acid composition discriminates between folded and intrinsically unstructured proteins. J. Mol. Biol. *347*, 827–839. https://doi.org/10.1016/j.jmb.2005.01.071.

59. Li, X., Romero, P., Rani, M., Dunker, A.K., and Obradovic, Z. (1999). Predicting Protein Disorder for N-C-and Internal Regions. Genome Inform. Ser. Workshop Genome Inform. *10*, 30–40.

60. Hu, G., Katuwawala, A., Wang, K., Wu, Z., Ghadermarzi, S., Gao, J., and Kurgan, L. (2021). flDPnn: Accurate intrinsic disorder prediction with putative propensities of disorder functions. Nat. Commun. *12*, 4438. https://doi.org/10.1038/s41467-021-24773-7.

61. Dayhoff, G.W., 2nd, and Uversky, V.N. (2022). Rapid prediction and analysis of protein intrinsic disorder. Protein Sci. *31*, e4496. https://doi.org/10.1002/pro.4496.

62. Hardenberg, M., Horvath, A., Ambrus, V., Fuxreiter, M., and Vendruscolo, M. (2020). Widespread occurrence of the droplet state of proteins in the human proteome. Proc. Natl. Acad. Sci. USA *117*, 33254–33262. https://doi.org/10.1073/pnas.2007670117.

63. Hatos, A., Tosatto, S.C.E., Vendruscolo, M., and Fuxreiter, M. (2022). FuzDrop on AlphaFold: visualizing the sequence-dependent propensity of liquid-liquid phase separation and aggregation of proteins. Nucleic Acids Res. *50*, W337–W344. https://doi.org/10.1093/nar/gkac386.

64. Oldfield, C.J., Cheng, Y., Cortese, M.S., Romero, P., Uversky, V.N., and Dunker, A.K. (2005). Coupled folding and binding with alpha-helix-forming molecular recognition elements. Biochemistry *44*, 12454–12470. https://doi.org/10.1021/bi050736e.

65. Dosztányi, Z., Meszaros, B., and Simon, I. (2009). ANCHOR: web server for predicting protein binding regions in disordered proteins. Bioinformatics *25*, 2745–2746. https://doi.org/10.1093/bioinformatics/btp518.

66. Mészáros, B., Simon, I., and Dosztanyi, Z. (2009). Prediction of protein binding regions in disordered proteins. PLoS Comput. Biol. *5*, e1000376. https://doi.org/10.1371/journal.pcbi.1000376.

67. Mohan, A., Oldfield, C.J., Radivojac, P., Vacic, V., Cortese, M.S., Dunker, A.K., and Uversky, V.N. (2006). Analysis of molecular recognition features (MoRFs). J. Mol. Biol. *362*, 1043–1059. https://doi.org/10.1016/j.jmb.2006.07.087.

68. Vacic, V., Oldfield, C.J., Mohan, A., Radivojac, P., Cortese, M.S., Uversky, V.N., and Dunker, A.K. (2007). Characterization of molecular recognition features, MoRFs, and their binding partners. J. Proteome Res. *6*, 2351–2366. https://doi.org/10.1021/pr0701411.

69. Cheng, Y., Oldfield, C.J., Meng, J., Romero, P., Uversky, V.N., and Dunker, A.K. (2007). Mining alpha-helix-forming molecular recognition features with cross species

sequence alignments. Biochemistry *46*, 13468–13477. https://doi.org/10.1021/bi7012273.

70. Drescher, M. (2012). EPR in protein science : intrinsically disordered proteins. Top. Curr. Chem. *321*, 91–119. https://doi.org/10.1007/128_2011_235.

71. Longhi, S., Belle, V., Fournel, A., Guigliarelli, B., and Carrière, F. (2011). Probing structural transitions in both structured and disordered proteins using site-directed spin-labeling EPR spectroscopy. J. Pept. Sci. *17*, 315–328. https://doi.org/10.1002/psc.1344.

72. Habchi, J., Tompa, P., Longhi, S., and Uversky, V.N. (2014). Introducing protein intrinsic disorder. Chem. Rev. *114*, 6561–6588. https://doi.org/10.1021/cr400514h.

73. Bernadó, P., and Svergun, D.I. (2012). Structural analysis of intrinsically disordered proteins by small-angle X-ray scattering. Mol. Biosyst. *8*, 151–167. https://doi.org/10.1039/c1mb05275f.

74. Bernado, P., and Svergun, D.I. (2012). Analysis of intrinsically disordered proteins by small-angle X-ray scattering. Methods Mol. Biol. *896*, 107–122. https://doi.org/10.1007/978-1-4614-3704-8_7.

75. Bernadó, P., Mylonas, E., Petoukhov, M.V., Blackledge, M., and Svergun, D.I. (2007). Structural characterization of flexible proteins using small-angle X-ray scattering. J. Am. Chem. Soc. *129*, 5656–5664. https://doi.org/10.1021/ja069124n.

76. Zhang, F., Fan, Q., Ren, K., and Andreassen, P.R. (2009). PALB2 functionally connects the breast cancer susceptibility proteins BRCA1 and BRCA2. Mol. Cancer Res. *7*, 1110–1118. https://doi.org/10.1158/1541-7786.MCR-09-0123.

77. Riback, J.A., Bowman, M.A., Zmyslowski, A.M., Knoverek, C.R., Jumper, J.M., Hinshaw, J.R., Kaye, E.B., Freed, K.F., Clark, P.L., and Sosnick, T.R. (2017). Innovative scattering analysis shows that hydrophobic disordered proteins are expanded in water. Science *358*, 238–241. https://doi.org/10.1126/science.aan5774.

78. Clark, P.L., Plaxco, K.W., and Sosnick, T.R. (2020). Water as a Good Solvent for Unfolded Proteins: Folding and Collapse are Fundamentally Different. J. Mol. Biol. *432*, 2882–2889. https://doi.org/10.1016/j.jmb.2020.01.031.

79. Kirby, N., Cowieson, N., Hawley, A.M., Mudie, S.T., McGillivray, D.J., Kusel, M., Samardzic-Boban, V., and Ryan, T.M. (2016). Improved radiation dose efficiency in solution SAXS using a sheath flow sample environment. Acta Crystallogr. D Struct. Biol. *72*, 1254–1266. https://doi.org/10.1107/S2059798316017174.

80. Meisburger, S.P., Taylor, A.B., Khan, C.A., Zhang, S., Fitzpatrick, P.F., and Ando, N. (2016). Domain Movements upon Activation of Phenylalanine Hydroxylase Characterized by Crystallography and Chromatography-Coupled Small-Angle X-ray Scattering. J. Am. Chem. Soc. *138*, 6506–6516. https://doi.org/10.1021/jacs.6b01563.

81. Meisburger, S.P., Xu, D., and Ando, N. (2021). REGALS: a general method to deconvolve X-ray scattering data from evolving mixtures. IUCrJ *8*, 225–237. https://doi.org/10.1107/S2052252521000555.

82. Curtis, J.E., Raghunandan, S., Nanda, H., and Krueger, S. (2012). SASSIE: A program to study intrinsically disordered biological molecules and macromolecular ensembles using experimental scattering restraints. Comput. Phys. Commun. *183*, 382–389. https://doi.org/10.1016/j.cpc.2011.09.010.

83. Mirdita, M., Schütze, K., Moriwaki, Y., Heo, L., Ovchinnikov, S., and Steinegger, M. (2022). ColabFold: making protein folding accessible to all. Nat. Methods *19*, 679–682. https://doi.org/10.1038/s41592-022-01488-1.

84. Yang, H., Zhou, C., Dhar, A., and Pavletich, N.P. (2020). Mechanism of strand exchange from RecA-DNA synaptic and D-loop structures. Nature *586*, 801–806. https://doi.org/10.1038/s41586-020-2820-9.

85. Chen, Z., Yang, H., and Pavletich, N.P. (2008). Mechanism of homologous recombination from the RecA-ssDNA/dsDNA structures. Nature *453*, 489–494. https://doi.org/10.1038/nature06971.

86. Ogawa, T., Yu, X., Shinohara, A., and Egelman, E.H. (1993). Similarity of the yeast RAD51 filament to the bacterial RecA filament. Science *259*, 1896–1899.

87. Grimme, J.M., Honda, M., Wright, R., Okuno, Y., Rothenberg, E., Mazin, A.V., Ha, T., and Spies, M. (2010). Human Rad52 binds and wraps single-stranded DNA and mediates annealing via two hRad52-ssDNA complexes. Nucleic Acids Res. *38*, 2917–2930. https://doi.org/10.1093/nar/gkp1249.

88. Kudryavtsev, V., Sikor, M., Kalinin, S., Mokranjac, D., Seidel, C.A.M., and Lamb, D.C. (2012). Combining MFD and PIE for accurate single-pair Forster resonance energy transfer measurements. ChemPhysChem *13*, 1060–1078. https://doi.org/10.1002/cphc.201100822.

89. Chinnaraj, M., Flaumenhaft, R., and Pozzi, N. (2022). Reduction of protein disulfide isomerase results in open conformations and stimulates dynamic exchange between structural ensembles. J. Biol. Chem. *298*, 102217. https://doi.org/10.1016/j.jbc.2022.102217.

90. Pozzi, N., Bystranowska, D., Zuo, X., and Di Cera, E. (2016). Structural Architecture of Prothrombin in Solution Revealed by Single Molecule Spectroscopy. J. Biol. Chem. *291*, 18107–18116. https://doi.org/10.1074/jbc.M116.738310.

91. Kapanidis, A.N., Lee, N.K., Laurence, T.A., Doose, S., Margeat, E., and Weiss, S. (2004). Fluorescence-aided molecule sorting: analysis of structure and interactions by alternating-laser excitation of single molecules. Proc. Natl. Acad. Sci. USA *101*, 8936–8941. https://doi.org/10.1073/pnas.0401690101.

92. Murphy, M.C., Rasnik, I., Cheng, W., Lohman, T.M., and Ha, T. (2004). Probing single-stranded DNA conformational flexibility using fluorescence spectroscopy. Biophys. J. *86*, 2530–2537. https://doi.org/10.1016/S0006-3495(04)74308-8.

93. Vancraenenbroeck, R., Harel, Y.S., Zheng, W., and Hofmann, H. (2019). Polymer effects modulate binding affinities in disordered proteins. Proc. Natl. Acad. Sci. USA *116*, 19506–19512. https://doi.org/10.1073/pnas.1904997116.

94. Mark, W.Y., Liao, J.C.C., Lu, Y., Ayed, A., Laister, R., Szymczyna, B., Chakrabartty, A., and Arrowsmith, C.H. (2005). Characterization of segments from the central region of BRCA1: an intrinsically disordered scaffold for multiple protein-protein and protein-DNA interactions? J. Mol. Biol. *345*, 275–287. https://doi.org/10.1016/j.jmb.2004.10.045.

95. Paull, T.T., Cortez, D., Bowers, B., Elledge, S.J., and Gellert, M. (2001). Direct DNA binding by Brca1. Proc. Natl. Acad. Sci. USA *98*, 6086–6091. https://doi.org/10.1073/pnas.111125998.

96. Naseem, R., Sturdy, A., Finch, D., Jowitt, T., and Webb, M. (2006). Mapping and conformational characterization of the DNA-binding region of the breast cancer susceptibility protein BRCA1. Biochem. J. *395*, 529–535. https://doi.org/10.1042/BJ20051646.

97. Yang, H., and Pavletich, N.P. (2021). Insights into homology search from cryo-EM structures of RecA-DNA recombination intermediates. Curr. Opin. Genet. Dev. *71*, 188–194. https://doi.org/10.1016/j.gde.2021.09.002.

98. Rothenberg, E., Grimme, J.M., Spies, M., and Ha, T. (2008). Human Rad52-mediated homology search and annealing occurs by continuous interactions between overlapping nucleoprotein complexes. Proc. Natl. Acad. Sci. USA *105*, 20274–20279. https://doi.org/10.1073/pnas.0810317106.

99. Feng, L.L., Bie, S.Y., Deng, Z.H., Bai, S.M., Shi, J., Qin, C.L., Liu, H.L., Li, J.X., Chen, W.Y., Zhou, J.Y., et al. (2024). Ubiquitin-induced RNF168 condensation promotes DNA double-strand break repair. Proc. Natl. Acad. Sci. USA *121*, e2322972121. https://doi.org/10.1073/pnas.2322972121.

100. Porro, A., and Sartori, A.A. (2019). Context Matters: RNF168 Connects with PALB2 to Rewire Homologous Recombination in BRCA1 Haploinsufficiency. Mol. Cell *73*, 1089–1091. https://doi.org/10.1016/j.molcel.2019.03.005.

101. Luijsterburg, M.S., Typas, D., Caron, M.C., Wiegant, W.W., van den Heuvel, D., Boonen, R.A., Couturier, A.M., Mullenders, L.H., Masson, J.Y., and van Attikum, H. (2017). A PALB2-interacting domain in RNF168 couples homologous recombination to DNA break-induced chromatin ubiquitylation. Elife *6*, e20922. https://doi.org/10.7554/eLife.20922.

102. Qin, C., Wang, Y.L., Zhou, J.Y., Shi, J., Zhao, W.W., Zhu, Y.X., Bai, S.M., Feng, L.L., Bie, S.Y., Zeng, B., et al. (2023). RAP80 phase separation at DNA double-strand break promotes BRCA1 recruitment. Nucleic Acids Res. *51*, 9733–9747. https://doi.org/10.1093/nar/gkad686.

103. Redington, J., Deveryshetty, J., Kanikkannan, L., Miller, I., and Korolev, S. (2021). Structural Insight into the Mechanism of PALB2 Interaction with MRG15. Genes *12*, 2002. https://doi.org/10.3390/genes12122002.

104. Hayakawa, T., Zhang, F., Hayakawa, N., Ohtani, Y., Shinmyozu, K., Nakayama, J.i., and Andreassen, P.R. (2010). MRG15 binds directly to PALB2 and stimulates homology-directed repair of chromosomal breaks. J. Cell Sci. *123*, 1124–1130. https://doi.org/10.1242/jcs.060178.

105. Sy, S.M.H., Huen, M.S.Y., and Chen, J. (2009). MRG15 is a novel PALB2-interacting factor involved in homologous recombination. J. Biol. Chem. *284*, 21127–21131. https://doi.org/10.1074/jbc.C109.023937.

106. Chen, M., Takano-Maruyama, M., Pereira-Smith, O.M., Gaufo, G.O., and Tominaga, K. (2009). MRG15, a component of HAT and HDAC complexes, is essential for proliferation and differentiation of neural

precursor cells. J. Neurosci. Res. *87*, 1522–1531. https://doi.org/10.1002/jnr.21976.

107. Bleuyard, J.Y., Fournier, M., Nakato, R., Couturier, A.M., Katou, Y., Ralf, C., Hester, S.S., Dominguez, D., Rhodes, D., Humphrey, T.C., et al. (2017). MRG15-mediated tethering of PALB2 to unperturbed chromatin protects active genes from genotoxic stress. Proc. Natl. Acad. Sci. USA *114*, 7671–7676. https://doi.org/10.1073/pnas.1620208114.

108. Stortz, M., Presman, D.M., and Levi, V. (2024). Transcriptional condensates: a blessing or a curse for gene regulation? Commun. Biol. *7*, 187. https://doi.org/10.1038/s42003-024-05892-5.

109. Todd, M.J., Lorimer, G.H., and Thirumalai, D. (1996). Chaperonin-facilitated protein folding: optimization of rate and yield by an iterative annealing mechanism. Proc. Natl. Acad. Sci. USA *93*, 4030–4035. https://doi.org/10.1073/pnas.93.9.4030.

110. Bhaskaran, H., and Russell, R. (2007). Kinetic redistribution of native and misfolded RNAs by a DEAD-box chaperone. Nature *449*, 1014–1018. https://doi.org/10.1038/nature06235.

111. Rajkowitsch, L., and Schroeder, R. (2007). Dissecting RNA chaperone activity. RNA *13*, 2053–2060. https://doi.org/10.1261/rna.671807.

112. Michelini, F., Pitchiaya, S., Vitelli, V., Sharma, S., Gioia, U., Pessina, F., Cabrini, M., Wang, Y., Capozzo, I., Iannelli, F., et al. (2017). Damage-induced lncRNAs control the DNA damage response through interaction with DDRNAs at individual double-strand breaks. Nat. Cell Biol. *19*, 1400–1411. https://doi.org/10.1038/ncb3643.

113. Storici, F., Bebenek, K., Kunkel, T.A., Gordenin, D.A., and Resnick, M.A. (2007). RNA-templated DNA repair. Nature *447*, 338–341. https://doi.org/10.1038/nature05720.

114. Wei, W., Ba, Z., Gao, M., Wu, Y., Ma, Y., Amiard, S., White, C.I., Rendtlew Danielsen, J.M., Yang, Y.G., and Qi, Y. (2012). A role for small RNAs in DNA double-strand break repair. Cell *149*, 101–112. https://doi.org/10.1016/j.cell.2012.03.002.

115. Wang, C., Uversky, V.N., and Kurgan, L. (2016). Disordered nucleome: Abundance of intrinsic disorder in the DNA- and RNA-binding proteins in 1121 species from Eukaryota, Bacteria and Archaea. Proteomics *16*, 1486–1498. https://doi.org/10.1002/pmic.201500177.

116. Masuzawa, T., and Oyoshi, T. (2020). Roles of the RGG Domain and RNA Recognition Motif of Nucleolin in G-Quadruplex Stabilization. ACS Omega *5*, 5202–5208. https://doi.org/10.1021/acsomega.9b04221.

117. von Nicolai, C., Ehlén, Å., Martin, C., Zhang, X., and Carreira, A. (2016). A second DNA binding site in human BRCA2 promotes homologous recombination. Nat. Commun. *7*, 12813. https://doi.org/10.1038/ncomms12813.

118. Keskin Karakoyun, H., Yüksel, Ş.K., Amanoglu, I., Naserikhojasteh, L., Yeşilyurt,

A., Yakıcıer, C., Timuçin, E., and Akyerli, C.B. (2023). Evaluation of AlphaFold structure-based protein stability prediction on missense variations in cancer. Front. Genet. *14*, 1052383. https://doi.org/10.3389/fgene.2023.1052383.

119. Zhao, W., Steinfeld, J.B., Liang, F., Chen, X., Maranon, D.G., Jian Ma, C., Kwon, Y., Rao, T., Wang, W., Sheng, C., et al. (2017). BRCA1-BARD1 promotes RAD51-mediated homologous DNA pairing. Nature *550*, 360–365. https://doi.org/10.1038/nature24060.

120. Antifeeva, I.A., Fonin, A.V., Fefilova, A.S., Stepanenko, O.V., Povarova, O.I., Silonov, S.A., Kuznetsova, I.M., Uversky, V.N., and Turoverov, K.K. (2022). Liquid-liquid phase separation as an organizing principle of intracellular space: overview of the evolution of the cell compartmentalization concept. Cell. Mol. Life Sci. *79*, 251. https://doi.org/10.1007/s00018-022-04276-4.

121. Alghoul, E., Basbous, J., and Constantinou, A. (2023). Compartmentalization of the DNA damage response: Mechanisms and functions. DNA Repair *128*, 103524. https://doi.org/10.1016/j.dnarep.2023.103524.

122. Miné-Hattab, J., Heltberg, M., Villemeur, M., Guedj, C., Mora, T., Walczak, A.M., Dahan, M., and Taddei, A. (2021). Single molecule microscopy reveals key physical features of repair foci in living cells. Elife *10*, e60577. https://doi.org/10.7554/eLife.60577.

123. Spegg, V., and Altmeyer, M. (2021). Biomolecular condensates at sites of DNA damage: More than just a phase. DNA Repair *106*, 103179. https://doi.org/10.1016/j.dnarep.2021.103179.

124. Kilic, S., Lezaja, A., Gatti, M., Bianco, E., Michelena, J., Imhof, R., and Altmeyer, M. (2019). Phase separation of 53BP1 determines liquid-like behavior of DNA repair compartments. EMBO J. *38*, e101379. https://doi.org/10.15252/embj.2018101379.

125. Dall'Agnese, G., Dall'Agnese, A., Banani, S.F., Codrich, M., Malfatti, M.C., Antoniali, G., and Tell, G. (2023). Role of condensates in modulating DNA repair pathways and its implication for chemoresistance. J. Biol. Chem. *299*, 104800. https://doi.org/10.1016/j.jbc.2023.104800.

126. Kleijwegt, C., Bressac, F., Seurre, C., Bouchereau, W., Cohen, C., Texier, P., Simonet, T., Schaeffer, L., Lomonte, P., and Corpet, A. (2023). Interplay between PML NBs and HIRA for H3.3 dynamics following type I interferon stimulus. Elife *12*, e80156. https://doi.org/10.7554/eLife.80156.

127. Pavlova, I., Iudin, M., Surdina, A., Severov, V., and Varizhuk, A. (2023). G-Quadruplexes in Nuclear Biomolecular Condensates. Genes *14*, 1076. https://doi.org/10.3390/genes14051076.

128. Scalisi, S., Ahmad, A., D'Annunzio, S., Rousseau, D., and Zippo, A. (2023). Quantitative Analysis of PcG-Associated Condensates by Stochastic Optical Reconstruction Microscopy (STORM). Methods Mol. Biol. *2655*, 183–200. https://doi.org/10.1007/978-1-0716-3143-0_14.

129. Gibson, B.A., Blaukopf, C., Lou, T., Chen, L., Doolittle, L.K., Finkelstein, I., Narlikar, G.J., Gerlich, D.W., and Rosen, M.K. (2023). In diverse conditions, intrinsic chromatin condensates have liquid-like material properties. Proc. Natl. Acad. Sci. USA *120*, e2218085120. https://doi.org/10.1073/pnas.2218085120.

130. Schrimpf, W., Barth, A., Hendrix, J., and Lamb, D.C. (2018). PAM: A Framework for Integrated Analysis of Imaging, Single-Molecule, and Ensemble Fluorescence Data. Biophys. J. *114*, 1518–1528. https://doi.org/10.1016/j.bpj.2018.02.035.

131. Hopkins, J.B. (2023). BioXTAS RAW 2: new developments for a free open-source program for small angle scattering data reduction and analysis. Preprint at bioRxiv. https://doi.org/10.1101/2023.09.25.559353.

132. Schuck, P. (2000). Size-distribution analysis of macromolecules by sedimentation velocity ultracentrifugation and lamm equation modeling. Biophys. J. *78*, 1606–1619. https://doi.org/10.1016/S0006-3495(00)76713-0.

133. Dastvan, R., Rasouli, A., Dehghani-Ghahnaviyeh, S., Gies, S., and Tajkhorshid, E. (2022). Proton-driven alternating access in a spinster lipid transporter. Nat. Commun. *13*, 5161. https://doi.org/10.1038/s41467-022-32759-2.

134. Dastvan, R., Mishra, S., Peskova, Y.B., Nakamoto, R.K., and McHaourab, H.S. (2019). Mechanism of allosteric modulation of P-glycoprotein by transport substrates and inhibitors. Science *364*, 689–692. https://doi.org/10.1126/science.aav9406.

135. Dastvan, R., Fischer, A.W., Mishra, S., Meiler, J., and McHaourab, H.S. (2016). Protonation-dependent conformational dynamics of the multidrug transporter EmrE. Proc. Natl. Acad. Sci. USA *113*, 1220–1225. https://doi.org/10.1073/pnas.1520431113.

136. Hustedt, E.J., Stein, R.A., and McHaourab, H.S. (2021). Protein functional dynamics from the rigorous global analysis of DEER data: Conditions, components, and conformations. J. Gen. Physiol. *153*, e201711954. https://doi.org/10.1085/jgp.201711954.

137. Polyhach, Y., Bordignon, E., and Jeschke, G. (2011). Rotamer libraries of spin labelled cysteines for protein studies. Phys. Chem. Chem. Phys. *13*, 2356–2366. https://doi.org/10.1039/c0cp01865a.

138. Ruben, E., Planer, W., Chinnaraj, M., Chen, Z., Zuo, X., Pengo, V., De Filippis, V., Alluri, R.K., McCrae, K.R., Macor, P., et al. (2020). The J-elongated conformation of beta2-glycoprotein I predominates in solution: implications for our understanding of antiphospholipid syndrome. J. Biol. Chem. *295*, 10794–10806. https://doi.org/10.1074/jbc.RA120.013939.

139. Ferreon, A.C.M., Moran, C.R., Gambin, Y., and Deniz, A.A. (2010). Single-molecule fluorescence studies of intrinsically disordered proteins. Methods Enzymol. *472*, 179–204. https://doi.org/10.1016/S0076-6879(10)72010-3.

STAR★METHODS

KEY RESOURCES TABLE

REAGENT or RESOURCE	SOURCE	IDENTIFIER
Bacterial and virus strains		
BL21 Star™ (DE3) Chemically Competent E. coli	Thermo Fisher	Cat# C601003
Chemicals, peptides, and recombinant proteins		
PALB2 amino acids 1–195 - W	This paper	N/A
Terrific Broth	Thermo Fisher	Cat# 22711022
IPTG	Thermo Fisher	Cat# 15529019
CHAPS	Thermo Fisher	Cat# 28300
TCEP	Thermo Fisher	Cat# T2556
Brij35	Thermo Fisher	Cat# 85117
Ulp1 (SUMO Protease)	Thermo Fisher	Cat# 12588018
TEV Protease	Thermo Fisher	Cat# 12575015
EDTA	Thermo Fisher	Cat# 17892
NP40	Thermo Fisher	Cat# 85124
Maltose	Thermo Fisher	Cat# A16266.36
Tris base	Thermo Fisher	Cat# 17926
DMSO	Thermo Fisher	Cat# J66650.AK
NaH_2PO_4	Thermo Fisher	Cat# 207802500
Na_2HPO_4	Thermo Fisher	Cat# A11817.30
NaF	Thermo Fisher	Cat# 447355000
Tween 20	Thermo Fisher	Cat# 003005
PMSF Protease Inhibitor	Thermo Fisher	Cat# 36978
Amylose resin	New England Biolabs	Cat# E8021L
HEPES	Thermo Fisher	Cat# 11344041
MTSSL	Millipore Sigma	Cat# SML3037-5MG
Glycerol	Thermo Fisher	Cat# 15514029
NaCl	Thermo Fisher	Cat# 447302500
Critical commercial assays		
QuikChange Site-Directed Mutagenesis Kit	Agilent	Cat# 200518
Zeba Spin desalting column	Thermo Scientific	Cat# 89883
Deposited data		
SAXS scattering data for PALB2-DBD at 0.5 NaCl	www.sasbdb.org	SASDSZ5
SAXS scattering data for PALB2-DBD at 0.16 NaCl	www.sasbdb.org	SASDS26
SAXS scattering data for PALB2-DBD L24A mutant at 0.16 NaCl	www.sasbdb.org	SASDVQ7
SAXS scattering data for PALB2-DBD complex with dT50 at 0.16 NaCl	www.sasbdb.org	SASDVR7
Full SASSIE Monte Carlo structural ensembles for unguided and guided dimers and for L24A monomer	Zendo.org	https://doi.org/10.5281/zenodo.13892101
Oligonucleotides		
poly(dT)50	DNA Technologies (IDTDNA) Inc	Custom order
Cy3-poly(dT)50-Cy5	DNA Technologies (IDTDNA) Inc	Custom order

Continued

REAGENT or RESOURCE	SOURCE	IDENTIFIER
poly(dT)22	DNA Technologies (IDTDNA) Inc	Custom order
Recombinant DNA		
pSMT-MBP-PB2-195W	This paper	N/A
Software and algorithms		
MATLAB	MathWorks	https://www.mathworks.com/products/matlab.html
PAM module for MATLAB	Schrimpf et al.[130]	https://pam.readthedocs.io/en/latest/
GraphPad Prism	Prism	https://www.graphpad.com/
SymPhoTime software 64, version 2.4	PicoQuant	https://www.picoquant.com/products/category/software/symphotime-64-fluorescence-lifetime-imaging-and-correlation-software
ASTRA 7	Wyatt	https://www.wyatt.com/products/software/astra.html
BioXTAS RAW 2.1.1	Hopkins et al.[131]	https://bioxtas-raw.readthedocs.io/en/v2.1.1/install.html
Sedfit	Schuck et al.[132]	https://sedfitsedphat.github.io/
Sednterp	Philio et al.	http://www.jphilo.mailway.com/sednterp.htm

METHOD DETAILS

Cloning and purification

PALB2 N-terminal fragments (1–195 I195W) was cloned into a pSMT-MBP plasmid containing an N-terminal 6✕His-SUMO and a C-terminal MBP tag using Gibson assembly. The pSMT-MBP plasmid was created from a pET28b$^+$–based pSMT3 plasmid (gift of Dr. R. A. Kovall, University of Cincinnati) by insertion of a TEV cleavage site and MBP at the ORF C-terminus. Mutations were introduced using the Stratagene QuikChange protocol. All constructs were fully sequenced and verified. Constructs were transformed into BL21* cells for expression. Cell cultures were grown in TB to OD_{600} = 1.6, and protein expression was induced by 0.2 mM IPTG overnight at 16°C. Cell suspensions were centrifuged at 4,000 rpm for 15 min. Cell pellets were resuspended in lysis buffer (25 mM HEPES pH 8.0, 1 M NaCl, 10% glycerol, 2 mM CHAPS, 1 mM TCEP, 0.3% Brij35, 2 mM EDTA, 1 mM PMSF), frozen in liquid nitrogen, and stored at −80°C. Frozen cell suspension was thawed and lysed with lysozyme at 0.25 mg/mL for 20 min at room temperature, followed by three rounds of sonication (50% output and 50% pulsar setting for 4 min). Cell debris was removed by centrifugation at 30,600 *g* for 45 min. Supernatant was loaded onto an amylose resin column (New England Biolabs) equilibrated with binding buffer (25 mM HEPES pH 8.0, 1 M NaCl, 10% glycerol, 2 mM CHAPS, 1 mM TCEP). Resin was washed with binding buffer containing 0.05% NP40 and 1 mM EDTA, followed by a second wash with low-salt buffer (50 mM NaCl, 25 mM HEPES pH 8.0, 1 mM TCEP, 2 mM CHAPS, 0.2% NP40, 1 mM EDTA). Protein was eluted in a binding buffer containing 20 mM maltose. SUMO and MBP tags were cleaved using Ulp1 and TEV proteases, respectively. Protein was diluted 5-fold with binding buffer without NaCl to bring the NaCl concentration to 200 mM, loaded onto a Hi-Trap heparin affinity column (2 × 5 mL, GE Life Sciences), and eluted with a salt gradient (200–800 mM NaCl). Protein eluted from the column in the ∼600 mM NaCl fraction. Gel filtration was performed using a Superdex-200 10/300GL column (GE Life Sciences).

All DNA substrates were synthesized by Integrated DNA Technologies (IDTDNA) Inc.

Circular dichroism (CD)

A Zeba Spin desalting column (Thermo Scientific) was used to exchange protein buffer to buffer containing 10 mM $NaPO_4$, 150 mM NaF, 2 mM CHAPS. Samples were centrifuged at 16,000 *g* to remove aggregates, and the final concentration was verified. Measurements were performed using a Jasco J-715. Four samples were used for CD measurements: (1) 30 μM PALB2-DBD, (2) 30 μM Δ40-DBD, (3) 30 μM PALB2-DBD with 30 μM dT_{50}, and (4) 30 μM Δ40-DBD with 30 μM dT_{50}. Each spectrum is an average of 10 scans.

Electron paramagnetic resonance (EPR) analysis

Monocysteine PALB2 mutant proteins were labeled with MTSSL [S-(1-oxyl-2,2,5,5-tetramethyl-2,5-dihydro-1H-pyrrol-3-yl)methyl methanesulfonothioate] in a sample free of reducing agents. Unbound label was separated on a Superdex-200 10/300 gel filtration column. Spectra were measured using 30 μM protein in 20 mM Tris-acetate pH 7.0, 100 mM NaCl, 10% DMSO, and 5% glycerol with or without 60 μM dT_{40}. Continuous wave EPR spectroscopy (cwEPR) was performed on an EMX spectrometer operating at X-band frequency (9.77 GHz) at room temperature. A dielectric resonator (ER4123D) and 25 μL borosilicate glass capillaries were used. The center field was set to 3474 G and the sweep width was 150 G. The modulation amplitude, microwave power, and resolution were set to 1.6 G, 2 mW, and 1125 points, respectively.

Distance measurements are obtained using a Bruker 580 pulsed EPR spectrometer operating at Q-band frequencies (34 GHz) using DEER with a standard four-pulse protocol as in previous publications.[133–135] Glycerol is added to samples as a cryoprotectant, and DEER experiments are performed at 83 K. Primary DEER decay was analyzed using a home-written software operating in the MATLAB (MathWorks) environment as previously described.[136] Comparison of the experimental distance distribution with the NMR structure[47] using a rotamer library approach was facilitated by the MMM 2018.2 software package.[137] Rotamer library calculation was conducted at 298 K.

SEC-MALS-SAXS analysis

SAXS was performed at BioCAT (beamline 18ID at the Advanced Photon Source, Chicago) with in-line size exclusion chromatography (SEC) to separate sample from aggregates and other contaminants, thereby ensuring optimal sample quality. Multiangle light scattering (MALS), dynamic light scattering (DLS), and refractive index measurement (RI) were used for additional biophysical characterization (SEC-MALS-SAXS). All samples were centrifuged at 16,000 rpm for 10 min immediately prior to loading on the chromatography system, and were then loaded on a Superdex 200 Increase 10/300 GL column (Cytiva) run by 1260 Infinity II HPLC (Agilent Technologies) at 0.6 mL/min. The flow passed through (in order) the Agilent UV detector, a MALS/DLS detector (DAWN Helios II, Wyatt Technologies), and an RI detector (Optilab T-rEX, Wyatt). The flow then passed through the SAXS flow cell. The flow cell consists of a 1.0 mm ID quartz capillary with ~20 μm walls. A coflowing buffer sheath is used to separate samples from the capillary walls, helping prevent radiation damage (Kirby et al., 2016). X-ray data were collected using a 150 (h) × 25 (v) (μm) 12 keV beam, and scattering intensity was recorded using an Eiger2 XE 9M (Dectris) photon-counting detector. The detector was placed 3.6 m from the sample giving access to a q-range of 0.0029 Å^{-1} to 0.417 Å^{-1}, with the momentum transfer vector q defined as $q = (4\pi/\lambda)\sin(\theta)$. Exposures (0.5 s) were acquired every 1 s during elution, and data were reduced using BioXTAS RAW 2.1.1.[131] Buffer blanks were created by averaging regions flanking the elution peak and subtracted from exposures selected from the elution peak to create the I(q) vs. q curves used for subsequent analyses. Molecular weights and hydrodynamic radii were calculated from the MALS and DLS data, respectively, using ASTRA 7 software (Wyatt). Further experimental details and data analysis parameters can be found in the Supplementary Tables.

Additional SAXS experiments were performed at the ID7A beamline at the Cornell High Energy Synchrotron Source (CHESS, Ithaca, NY) using similar SEC-MALS-SAXS setup and identical sample preparation procedure. SEC was performed using a Superdex 200 Increase 10/300 GL column (Cytiva) run by a Teledyne Reaxus HPLC pump at 0.6 mL/min. X-ray data were collected using a 250 (h) × 250 (v) (μm) 11.3 keV beam, and scattering intensity was recorded using an Eiger 4M (Dectris) photon-counting detector. The detector was placed 1.78 m from the sample giving access to a q-range of 0.0083 Å^{-1} to 0.44 Å^{-1}, with the momentum transfer vector q defined as $q = (4\pi/\lambda)\sin(\theta)$. Exposures (1 s) were acquired every 1 s during elution, and data were reduced using BioXTAS RAW 2.2.1.[131] Buffer blanks were created by averaging regions preceding the elution peak. Deconvolution by EFA[80] and/or REGALS[81] was performed to separate out the component of interest from other species and accumulated radiation damage. Molecular weights and hydrodynamic radii were calculated from the MALS and DLS data, respectively, using ASTRA 7 software (Wyatt).

Confocal smFRET analysis

All samples were prepared in buffer (0.16 M NaCl, 20 mM HEPES pH 7.5, 1 mM TCEP, 0.003% Tween 20) and centrifuged at 40,000 rpm for 20 min before the experiment. FRET measurements of freely diffusing single molecules were performed with a confocal microscope [MicroTime 200 (PicoQuant)] as described previously.[90,138] The donor and acceptor were excited by light from 532 nm to 638 nm lasers, respectively. A pulsed interleaved excitation (PIE) setup was used with a pulse rate of 40 MHz to alternate donor and acceptor excitation. PIE reports the status of both donor and acceptor fluorophores by sorting molecules based on relative donor:acceptor stoichiometry (S) and apparent FRET efficiency (E) as described previously.[88,91,139] Measurements were performed 25-μm deep in the solution using a laser power of ~15 μW for 30–60 min per sample. Data were recorded using SymPhoTime software 64, version 2.4 (PicoQuant). Data were analyzed with MATLAB-based PAM software (https://pam.readthedocs.io/en/latest/)[130] using a customized profile optimized for our microscope. Signals from single molecules were observed as bursts of fluorescence. Bursts with more than 50 counts were searched with the dual channel burst search (DCBS) algorithm. Integration time was set to 0.5 ms. Appropriate corrections for direct excitation of the acceptor at the donor excitation wavelength (DE), leakage of the donor in the acceptor channel (Lk), and the instrumental factor (g) were determined experimentally using a mixture of dsDNA models with known FRET efficiency and stoichiometry labeled with Cy3 and Cy5: DE = 0.05, Lk = 0.08, g = 0.85.

Analytical ultracentrifugation (AUC)

PALB2-DBD samples (1 mL) were dialyzed against 0.5 L of buffer (0.16 M NaCl, 25 mM HEPES pH 7.5, 1 mM TCEP) in dialysis bags for 4 h at room temperature. The sample was centrifuged at 14,000 rpm for 5 min at room temperature and the concentration was measured by Bradford assay. Experiments were performed using a Beckman Coulter Optima AUC. Samples were loaded into cells and centrifuged at 40,000 rpm for 12 h at 21°C. Absorbance was measured at 280 nm for protein samples and at 550 nm for samples with Cy3-labeled DNA every 4 min for a total of 200 scans. Buffer density and viscosity were calculated using the Sednterp program data fitting was performed using the Lamm equation for the continuous c(s) distribution model in Sedfit.[132] DNA-only samples were analyzed using a spatial specific volume of 0.55.

Turbidity and droplets formation

Protein stock was dialyzed against buffer (0.2M NaCl, 25 mM HEPES pH 7.5, 1 mM TCEP), diluted in corresponding buffer to adjust the salt concentration to a desired value, incubated for 10 min and the turbidity was measured using SpectraMax i3 (Molecular Devices) at 600 nm wavelength in 384 well clear bottom non-binding surface plates (Corning) with total volume of 80 μL with total protein concentration of 4 μM. Solutions were incubated for an additional 30 min, the NaCl concentration was adjusted to 0.3M, and the turbidity was measured after 5 min incubation. Same solutions were imaged on Keyence BZ-X800 microscope after the initial incubation and after salt adjustment.

QUANTIFICATION AND STATISTICAL ANALYSIS

None outside of measurements generated by commercial software packages used for analysis of SAXS.